ULTRASHORT PULSE PROPAGATION IN THE LINEAR REGIME

A Thesis

by

JIEYU WANG

Submitted to the Office of Graduate Studies of
Texas A&M University
in partial fulfillment of the requirements for the degree of

MASTER OF SCIENCE

December 2009

Major Subject: Physics

ULTRASHORT PULSE PROPAGATION IN THE LINEAR REGIME

A Thesis

by

JIEYU WANG

Submitted to the Office of Graduate Studies of
Texas A&M University
in partial fulfillment of the requirements for the degree of

MASTER OF SCIENCE

Approved by:

Chair of Committee,	George W. Kattawar
Committee Members,	Alexei V. Sokolov
	Ping Yang
Head of Department,	Edward S. Fry

December 2009

Major Subject: Physics

ABSTRACT

Ultrashort Pulse Propagation in the Linear Regime. (December 2009)

Jieyu Wang, B.S., University of Science and Technology of China

Chair of Advisory Committee: Dr. George W. Kattawar

First, we investigate the Bouguer-Lambert-Beer (BLB) law as applied to the transmission of ultrashort pulses through water in the linear absorption regime. We present a linear theory for propagation of ultrashort laser pulses, and related experimental results are in excellent agreement with this theory. Thus we conclude that recent claims of the BLB law violations are inconsistent with the experimental data obtained by our group.

Second, we study the dynamics of ultrashort pulses in a Lorentz medium and in water via the saddle point method. It shows that the saddle point method is a more efficient and faster method than the direct integration method to study one-dimensional pulse propagation over macroscopic distances (that is, distance comparable to the wavelength) in a general dielectric medium. Comments are also made about the exponential attenuation of the generalized Sommerfeld and Brillouin precursors. By applying the saddle point method, we also determined that the pulse duration estimated by the group velocity dispersion (GVD) approximation is within 2% of the value computed with the actual refractive index for a propagation distance of 6 m in water.

ACKNOWLEDGEMENTS

I would like to thank my committee chair, Dr. Kattawar, and my committee members, Dr. Sokolov, Dr. Yang, for their guidance and support throughout the course of this research.

Thanks also go to my friends and the department faculty and staff for making my time at Texas A&M University a great experience. I am also grateful to my colleagues, Pengwang, Zai, Yu You, Lei bi, Zhaokai Meng, Ben, and Lucas for their help in the course of study and research.

Finally, thanks to my mother and father for their encouragement.

TABLE OF CONTENTS

LIST OF FIGURES

FIGURE Page

CHAPTER I

INTRODUCTION AND BACKGROUND

A. Pioneering study of precursors

In Brillouin's book [1], *Wave Propagation and Group Velocity*, he used the word "forerunner" instead of the current widely accepted word "precursor" to describe the wave front of the electric fields which comes earlier than the main signal. In fact, the study of the details of pulse propagation in a linear dispersive medium was somewhat motivated by the debate of whether the speed of energy can be greater than the speed of light c.

Before the wide application of the ultrashort pulses and before the study on strong absorptive media, it was reasonable to define the signal velocity as the propagation velocity of the peak of the pulse, which coincides with the group velocity. Group velocity describes the velocity for the multi-chromatic light propagation in a linear dispersive and non-strong absorptive medium. For simplicity, one dimensional group velocity is defined as the following:

$$v_g = \frac{d\omega}{dk(\omega)} = \frac{c}{n(\omega) + \omega \dfrac{dn(\omega)}{d\omega}} = \frac{c}{n(\lambda) - \dfrac{dn(\lambda)}{d\lambda}\lambda}, \tag{1.1}$$

where c is the speed of light, ω is the angular frequency (hereafter referred to simply as frequency), $\lambda = \dfrac{2\pi c}{\omega}$ is the wavelength in vacuum, k is the wave vector and $n(\omega) = \dfrac{k(\omega)c}{\omega}$ is the refractive index of the medium. If we define the wave vector in

---

This thesis follows the style and format of Applied Optics.

vacuum as $k_0(\omega) = \frac{\omega}{c} = \frac{2\pi}{\lambda}$, then $n(\omega) = \frac{k(\omega)}{k_0(\omega)}$. The refractive index $n(\omega)$ is a function of frequency in a dispersive medium. In the strong anomalous dispersion regime, where $\frac{dn}{d\omega} < 0$, the predicted group velocity can be negative or greater than the speed of light for some frequencies. Chu and Wong's group [2] even measured a negative signal velocity and velocity greater than the light speed. C. G. B. Garrett and D. E. McCumber [3] and Crisp [4,5] showed that even when the group velocity is negative or greater than c, it is still capable of describing the signal velocity. They claimed that this seeming violation of causality is due to the pulse shape distortion. Also, they claimed the results don't violate special relativity because the signal peak propagation is different from the energy or the information propagation. Energy velocity v_E is a better quantity to describe information propagation, and it is defined as the rate of energy flow divided by the stored energy density [3]. London showed that the energy velocity is always less than c [6]. In a later paper, Xiao and Oughtsun [7] pointed out that, as the propagation distance increases, the accuracy of the asymptotic description of energy velocity increases while that of the group velocity description decreases. In many situations, a single concept of velocity is not enough to the describe pulse propagation due to pulse shape distortion. It is therefore necessary to obtain the details of the electric field information.

Brillouin studied the detailed dynamics of a step-modulated signal, which is generally composed of the forerunners and the main signal, in a Lorentz medium. Oughstun [8] made his own contribution to this field by using a modern asymptotic method, improving and correcting some comments in Brillouin's book.

It is stated that the medium needs time to be set into motion before it responds to the wave front, and thus the wave front propagates as it would in a vacuum. There are two types of precursors in [1]; the first is the Sommerfeld precursor of high frequency and the second is the Brillouin precursor of low frequency.

Precursors are again brought to attention because Choi and Österberg [9] claimed that they observed optical precursors in deionized water. Their measurements showed that the precursors are attenuated less than exponential with distance and therefore significantly more energy remains in the pulse after propagating through 5 m of water when compared with the predictions of the Bouguer-Lambert-Beer (BLB) law. If this claim were true, precursors make it possible to transmit light over much greater distances, which could be applied to underwater communication and remote sensing. In the later papers, Österberg' s group [10, 11] again stated that their data disagreed with the BLB law, while the experimental results of several other groups [12, 13] are consistent with the BLB law. To reconcile the two conflicting claims regarding pulse propagation in a linear medium and obtain an overall understanding of precursors, our group conducted well-designed experiments and performed detailed study of ultrashort pulse propagation.

B. Introduction to the methods of solving pulse propagation in the linear regime

The general Maxwell equations frequently used in a bulk medium are the macroscopic Maxwell equations [14]. They can be derived from the microscopic ones (the Maxwell equations in vacuum). The microscopic Maxwell equations in CGS unit are

$$\nabla \cdot \vec{b} = 0, \nabla \times \vec{e} + \frac{\partial \vec{b}}{\partial t} = 0$$

$$\nabla \cdot \vec{e} = \rho_v / \varepsilon_0, \nabla \times \vec{b} - \frac{1}{c^2}\frac{\partial \vec{e}}{\partial t} = \mu_0 \vec{J}_v \ , \tag{1.2}$$

where $\vec{e}$ and $\vec{b}$ are the microscopic electric and magnetic fields and ρ_v and $\vec{J}_v$ are the microscopic charges and current densities. The medium is considered to be a collection of moving point charges in vacuum, that is, a source of charges ρ_v and currents $\vec{J}_v$. A spatial average of the isolated atoms and the linear polarization approximation lead to the macroscopic Maxwell equations in a homogeneous and isotropic medium, where the whole medium is treated approximately as a continuous medium. The macroscopic Maxwell equations follow:

$$\begin{aligned} \nabla \cdot \vec{B} = 0, \nabla \times \vec{E} + \frac{\partial \vec{B}}{\partial t} = 0 \\ \nabla \cdot \vec{D} = \rho, \nabla \times \vec{H} - \frac{\partial \vec{D}}{\partial t} = \vec{J}, \end{aligned} \tag{1.3}$$

where $\vec{E}$ and $\vec{B}$ are the macroscopic electric and magnetic fields, $\vec{D}$ and $\vec{H}$ are the derived fields, which are related to $\vec{E}$ and $\vec{B}$ through the linear polarization $\vec{P}$ and magnetization $\vec{M}$ for mono-chromatic light:

$$\vec{D} = \varepsilon_0 \vec{E} + \vec{P}, \vec{H} = \frac{1}{\mu_0}\vec{B} - \vec{M} \ . \tag{1.4}$$

In the dielectric media we consider, the magnetization is neglected. $\vec{P}$ is proportional to $\vec{E}$, and we have

$$\vec{D} = \varepsilon \vec{E} \text{ and } \vec{H} = \frac{1}{\mu_0}\vec{B}. \tag{1.5}$$

The relationship between $\vec{D}$ and $\vec{E}$ depends on the frequency. For a certain frequency ω,

$$\vec{D}(\omega) = \varepsilon(\omega)\vec{E}(\omega). \tag{1.6}$$

Eq. (1.5) is valid only for monochromatic radiation. A pulse with a broad spectrum can be seen as a superposition of many harmonic waves. First, we can solve the electric propagation for a single frequency combining Eqs. (1.3) and (1.6) (i.e. solve the field in spectral space), and then apply the superposition method to obtain the total electric field. This is also a popular application of the Fourier transformation.

For a polarized plane wave propagating in the z direction, the Fourier component of the electric field $\vec{E}(z,\omega)$ satisfies the following equation:

$$\nabla^2 \vec{E}(z,\omega) + \mu_0 \varepsilon(\omega)\omega^2 \vec{E}(z,\omega) = 0, \tag{1.7}$$

where $k(\omega) = \omega\sqrt{\varepsilon(\omega)\mu_0}$. This equation is obtained through the Fourier transformation of Eq. (1.3) combined with the dispersion relationship (1.5) and (1.6). The solution of the polarized harmonic wave in the $z > 0$ half space is:

$$E(z,\omega) = E(0,\omega)\exp(i(k(\omega)z). \tag{1.8}$$

Here $E(0,\omega)$ is determined by the boundary condition. The intensity in spectral space, which is the square modulus of the above Fourier component, follows the BLB law directly:

$$I(\omega) = I_0(\omega)\exp(-\alpha(\omega)z), \tag{1.9}$$

where $\alpha(\omega) = 2\,\mathrm{Im}(k(\omega))$ is the absorption coefficient and $I_0(\omega) = E(0,\omega)E(0,\omega)^*$. Applying the inverse Fourier transformation or the superposition rule, the electric field in the time domain is:

$$E(z,t) = \int E(0,\omega)\exp(ik(\omega)z - i\omega t)d\omega\,. \tag{1.10}$$

Here $E(0,\omega)$ is the spectral amplitude or the Fourier component of the electric field at $z = 0$:

$$E(0,\omega) = \int E(0,t)\exp(i\omega t)dt\,. \tag{1.11}$$

Formula (1.10) is the basic formula we use to solve the one dimensional electric field propagation problem. Direct integration is sometimes difficult for a pulse with a broad spectrum traveling a long distance z, because the phase oscillates very fast. Therefore, asymptotic methods such as the saddle point method are used to solve Eq. (1.10) and to obtain analytic solutions. The saddle point method has been only applied to media with sharp peak absorptive lines [1, 8], and it turns out to be a very good method to solve pulse propagation problems in water, the refractive index of which is relatively flat.

An alternative way to solve the electric field is to deal with the equations in the time domain directly:

$$\nabla \times \vec{E} + \frac{\partial \vec{B}}{\partial t} = 0$$

$$\nabla \times \vec{H} - \frac{\partial \vec{D}}{\partial t} = 0 \qquad \text{(1.12 (a))}$$

$$\vec{D}(\vec{r},t) = \varepsilon_0[\vec{E}(\vec{r},t) + \int_0^t G(\tau)\vec{E}(\vec{r},t-\tau)d\tau]$$
$$G(\tau) = \frac{1}{2\pi}\int_{-\infty}^{\infty}[\varepsilon(\omega)/\varepsilon_0 - 1]e^{-i\omega\tau}d\omega. \qquad \text{(1.12 (b))}$$

Eq. (1.12 (a)) is derived from $\vec{D}(\omega) = \varepsilon(\omega)\vec{E}(\omega)$ via the Fourier transformation. The value of the $\vec{D}$ field at time t depends on the $\vec{E}$ field at all previous times. Eq. (1.12) is difficult to calculate numerically because the integration needs to be recalculated for each time step, and storage is required for $\vec{E}$ at all previous times. Auxiliary differential equation (ADE) method [15] is developed for the Debye and the Lorentz medium, when the convolution integration (Eq. (12)) is replaced by P linear first order equations for the P-pole Debye model (see Debye model below) and P second order equations for the P-pole Lorentz medium. For the one-pole Debye model,

$$\varepsilon(\omega) = \varepsilon_\infty + \frac{\varepsilon_s - \varepsilon_\infty}{1 - i\omega\tau}, \qquad (1.13)$$

where ε_∞ is the permittivity in the high frequency limit, ε_s is the static permittivity in the low frequency limit, and τ is the characteristic relaxation time of the medium. For a medium which has one or more real poles of separate frequencies, we have, for example, the P-pole Debye model,

$$\varepsilon(\omega) = \varepsilon_\infty + \sum_{p=1}^{P}\frac{\varepsilon_{sp} - \varepsilon_\infty}{1 - i\omega\tau_p}. \qquad (1.14)$$

Here ε_{sp} is the static permittivity in the low frequency limit and τ_p is the relaxation time for the p_{th} pole.

For simplicity, we describe how to obtain the ancillary differential equations for the 2-pole Debye model [15-17]. The permittivity of the 2-pole Debye model is shown in Eq. (1.15).

$$\varepsilon(\omega) = \varepsilon_\infty + \frac{\varepsilon_{s1} - \varepsilon_\infty}{1 - i\omega\tau_1} + \frac{\varepsilon_{s2} - \varepsilon_\infty}{1 - i\omega\tau_2}. \tag{1.15}$$

By replacing the permittivity expression in Eq. (1.13), we obtain:

$$\begin{aligned} D(\vec{r},t) &= \varepsilon_\infty E(\vec{r},t) + \frac{1}{\sqrt{2\pi}}\int_{-\infty}^{\infty}(\varepsilon(\omega) - \varepsilon_\infty)E(\vec{r},\omega)e^{-i\omega t}d\omega \\ &= \varepsilon_\infty E(\vec{r},t) + \frac{1}{\sqrt{2\pi}}\int_{-\infty}^{\infty}\frac{\varepsilon_{s1} - \varepsilon_\infty}{1 - i\omega\tau_1}E(\vec{r},\omega)e^{-i\omega t}d\omega + \frac{1}{\sqrt{2\pi}}\int_{-\infty}^{\infty}\frac{\varepsilon_{s2} - \varepsilon_\infty}{1 - i\omega\tau_2}E(\vec{r},\omega)e^{-i\omega t}d\omega. \end{aligned} \tag{1.16}$$

We then define

$$\begin{aligned} J_1(\vec{r},\omega) &= -i\omega\tau_1\frac{\varepsilon_{s1} - \varepsilon_\infty}{1 - i\omega\tau_1}E(\vec{r},\omega), \\ J_2(\vec{r},\omega) &= -i\omega\tau_2\frac{\varepsilon_{s2} - \varepsilon_\infty}{1 - i\omega\tau_2}E(\vec{r},\omega). \end{aligned} \tag{1.17}$$

In the time domain, we obtain the ancillary current via the Fourier transformation:

$$J_p(\vec{r},t) = \frac{1}{\sqrt{2\pi}}\int_{-\infty}^{\infty}J_p(\vec{r},\omega)e^{i\omega t}d\omega$$

$$\frac{\partial J_p(\vec{r},t)}{\partial t} = \frac{\varepsilon_{sp} - \varepsilon_\infty}{\tau_p}\frac{\partial E(\vec{r},t)}{\partial t} - \frac{1}{\tau_p}J_p(\vec{r},t), \text{ with } p = 1,2 . \tag{1.18}$$

Differentiating Eq. (1.16) with respect to time, we get

$$\frac{\partial D(\vec{r},t)}{\partial t} = \varepsilon_\infty\frac{\partial E(\vec{r},t)}{\partial t} + J_1(\vec{r},t) + J_2(\vec{r},t). \tag{1.19}$$

Finally, replacing $\frac{\partial D}{\partial t}$ in Eq. (1.12(a)) by Eq. (1.19) and replacing $\vec{r}$ by z, we obtain the equations for one dimensional electric field propagation in the z direction through a 2-pole Debye model, and we can then apply the FDTD method [15] and Discontinuous Galerkin (DG) method [18] to solve the equations.

$$\begin{aligned}
\frac{\partial H}{\partial t} &= -\frac{1}{\mu_0}\frac{\partial E}{\partial z}, \\
\frac{\partial E}{\partial t} &= \frac{1}{\varepsilon_\infty}\sum_{p=1}^{P} J_p + \frac{1}{\varepsilon_\infty}\frac{\partial H}{\partial z}, \\
\frac{\partial J_p}{\partial t} &= \frac{\varepsilon_{sp}-\varepsilon_\infty}{\tau_p}\frac{\partial E}{\partial t} - \frac{1}{\tau_p}J_p.
\end{aligned} \tag{1.20}$$

$p = 1,2$ for the two-pole and $p = 1,2,...,P$ for the P-pole Debye model. Similar results can be deduced for the Lorentz medium.

The advantage of the ADE method over the convolution integration (1.12 (b)) is significant when the dielectric properties of the medium we study can be expressed as a sum of the Debye or Lorentz models. For example, the permittivity of water [19] can be fit as Eq. (1.21) in a broad spectral regime:

$$\varepsilon(\omega) = \frac{\prod_{m=1}^{M}(\omega - Z_m)}{\prod_{m=1}^{M}(\omega - P_m)}, \tag{1.21}$$

where $\varepsilon(\omega)$ is the permittivity of water, Z_m is the m_{th} zero and P_m is the m_{th} pole of $\varepsilon(\omega)$. In total, there are M zeros and M poles in this example. In a practical calculation, the required spectral regime is relatively narrow, and we can get a more accurate fitting of the permittivity. The coefficients of the ancillary equations for the Debye medium are all real. A general complex permittivity can be written in the form of a summation:

$$\varepsilon(\omega) = \varepsilon_{\infty} + \sum_{p=1}^{P} \frac{a_p}{1 - j\omega b_p}, \tag{1.22}$$

with the complex coefficients a_p and b_p. The ADE method can be generalized to a larger group of dielectric media with permittivity in the form (1.22). Similar to the Debye medium (Eq. (1.17)), we have:

$$J_p(\vec{r},\omega) = -i\omega b_p \frac{a_p}{1 - i\omega b_p} E(\vec{r},\omega). \tag{1.23}$$

The only difference is that the coefficients in the equations for $J_p(\vec{r},t)$ are complex:

$$\frac{\partial J_p(\vec{r},t)}{\partial t} = \frac{a_p}{b_p}\frac{\partial E(\vec{r},t)}{\partial t} - \frac{1}{b_p} J_p(\vec{r},t). \tag{1.24}$$

We should separate the variable $J_p(\vec{r},t)$ into a real part $J_p(\vec{r},t)$ and an imaginary part $J_p(\vec{r},t)^{"}$, which results in 2P ancillary equations instead of P equations for the P-pole Deybe model.

C. Introduction to the saddle point method

When calculating the extreme values (maximum or minimum) of a one-dimensional function or a real variable function, we calculate the first derivative of the function. For example, in the two functions $f_1(x) = x^2$ and $f_2(x) = x^3$, $x = 0$ is the stationary point for the two equations satisfying the relation:

$$\frac{df_1(x)}{dx} = 2x = 0, \ \frac{df_2(x)}{dx} = 3x^2 = 0.$$

$f_1(x)$ reaches its minimum value at $x = 0$ while $f_2(x)$ does not, even though $\frac{df_2(x)}{dx} = 0$ at $x = 0$, as shown in Fig. (1.1(a)) . Thus $x = 0$ is the saddle point for $f_2(x)$.

For a complex function $\eta = \eta(\omega)$, where $\omega = x + iy$, x and y are the real part and imaginary part of ω, and $\eta(\omega) = u(\omega) + iv(\omega)$ where $u(\omega)$ and $v(\omega)$ are the real part and imaginary part of $\eta(\omega)$, respectively. When we differentiate a complex function, the difference from a real function is that for a complex function there are infinite paths in the complex plane to calculate the derivative (see Fig. 1(b)), while for the real variable function there is only one path which is along the real axis. The Cauchy-Riemann conditions guarantee the existence of the derivative of a complex function by requiring all the derivatives along any direction are the same:

$$\begin{aligned} \frac{\partial u}{\partial x} &= \frac{\partial v}{\partial y} \\ \frac{\partial u}{\partial y} &= -\frac{\partial v}{\partial x}. \end{aligned} \tag{1.25}$$

The Cauchy-Riemann conditions also limit the stationary points to be the saddle points but not the points at which the function reaches its extreme value. From the Cauchy-Riemann equations, we get

$$\frac{\partial^2 u}{\partial x^2} + \frac{\partial^2 u}{\partial y^2} = 0. \tag{1.26}$$

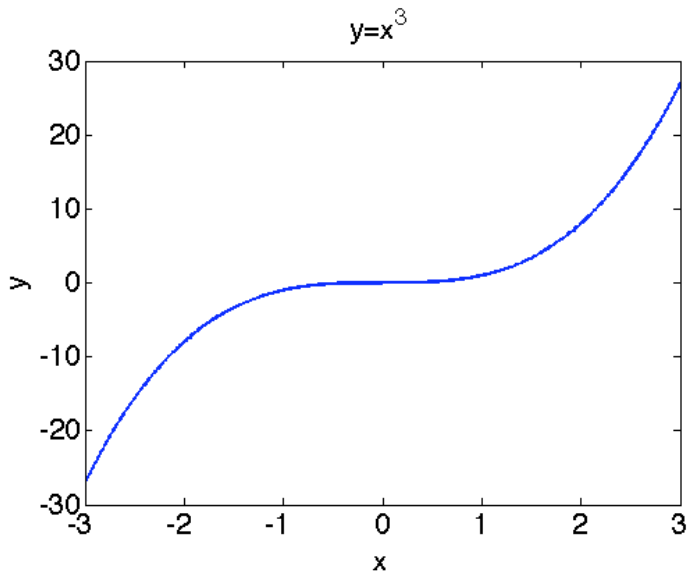

(a)

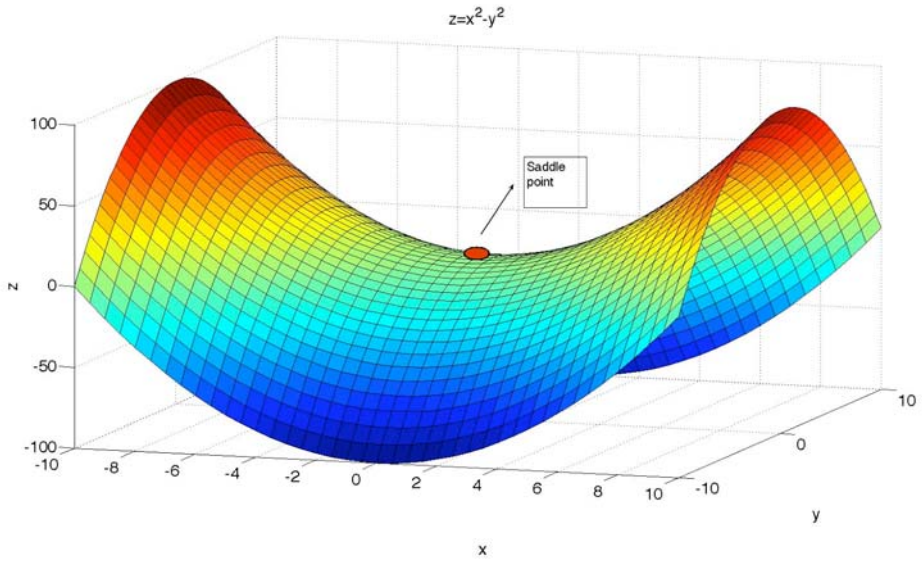

(b)

Fig. 1.1 (color online) Examples of saddle points.
(a) Example of the saddle point at $x = 0$ for $f_2(x) = x^3$.
(b) Example of the saddle point for $z = x^2 - y^2$.

The points satisfying the above condition are not extreme value points, because the equation indicates the curvatures (the second derivative at) at the stationary points

along the x direction and y direction are of different signs. For example, $\frac{\partial^2 u}{\partial x^2} > 0, \frac{\partial^2 u}{\partial y^2} < 0$, indicates that at the saddle point, the value of the function reaches a maximum along the y direction and a minimum along the x direction. Therefore, in the complex plane, a function doesn't obtain the extreme value over the complex plane, although for a special path (equivalent to a single variable function), it is possible to obtain the maximum or the minimum value.

For a integration below,

$$I = \int_{-\infty}^{\infty} \phi(\omega) g(\omega) d\omega = \int_{-\infty}^{\infty} \phi(\omega) e^{x\eta(\omega)} d\omega, \tag{1.27}$$

where $\phi(\omega)$ is a slowly changing function, and $g(\omega)$ is a fast changing function because it has a generalized phase $x\eta(\omega)$. x is a large real positive number and $\eta(\omega)$ is a complex function of ω. When dealing with integration of a function $g(\omega)$, it is straightforward to emphasize the regime where the real part of $\eta(\omega)$ (or $u(\omega)$) is large, because the exponential function and the large value of x make the outside regime significantly small compared with the function values within this regime. The natural way is to find the maximum value of $\eta(\omega)$ along the real axis (the original integration path). In the situation when there is no stationary point for $\eta(\omega)$ on the real axis but only in the complex plane, which is equivalent to $\frac{d\eta(\omega)}{d\omega} = 0$ having only complex solutions of ω, we try to deform the integration path to the complex plane. In the theory of contour integration, if there is no pole for the integration function $g(\omega)$:

$$I_c = \int_C g(\omega) d\omega = 0 \quad \text{or} \quad I = \int_{A(p1)}^{B(p1)} g(\omega) d\omega = \int_{A(p2)}^{B(p2)} g(\omega) d\omega. \tag{1.28}$$

As indicated in Fig. 1.2, C is the contour, A, B are any two different points in the contour. P1 indicates one path, and P2 indicates the other path. P1 and –P2 together form the contour.

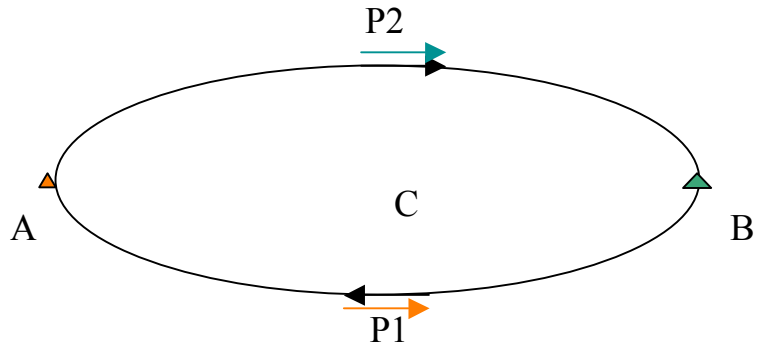

Fig. 1.2 (color online) Illustration of the contour path for complex integration. A, B are two points on the contour. P1 represents the path from A to B indicated by the yellow arrow and P2 represents the path from A to B indicated by the green arrow. C represents the contour indicated by the black arrow.

We have enough clues to deform the original integration on the real axis to a path in the complex plane which passes the saddle points. Next, we want to determine which path is the one we want. Since the function value changes quickly, it is reasonable to think that the integration should be along the path where the function value has the steepest descent near the saddle point. Along this path, the smallest range of integration is needed to achieve the same accuracy.

Also from the Cauchy-Riemann conditions, the level curves on u (where u is constant) and the level curves of v (where v is constant) are perpendicular. Therefore the steepest descent direction is along the path with constant v or with constant imaginary $\eta(\omega)$. That is to say, the phase is stationary along the steepest descent path near saddle points. Usually, the expression of path in the complex plane is an intricate function of ω,

which requires more work to calculate the integral. It is found that in many cases, it is an easier and just as accurate way to deform the path a little bit from the steepest descent direction [20], which is called the critical path, and then apply Taylor expansion to the generalized phase. The important advantage is that we obtain an analytic result with this method. The critical path can replace the steepest descent path only if the angle between the two paths is smaller than 90 degrees.

It is assumed here $\eta(\omega)$ can be expanded as a convergent power series and the series converge in the regime $|\omega-\omega_0|<R$. $a_j, j=1,2,...,\infty$ are the coefficients of the Taylor expansion (1.29).

$$\eta(\omega)=\eta(\omega_0)+a_2(\omega-\omega_0)^2+a_3(\omega-\omega_0)^3+.... \quad (1.29)$$

Keeping terms of up to second order, the integration is approximated by:

$$\int \phi(\omega)e^{x\eta(\omega)}d\omega \sim \phi(\omega_0)e^{x\eta(\omega_0)a_2}\int e^{xa_2(\omega-\omega_0)^2}d\omega . \quad (1.30)$$

The values of $a_2(\omega-\omega_0)^2$ are real and negative along the critical direction in the path near the saddle point ω_0. In the case $a_2=|a_2|e^{\alpha i}$, the path for ω near ω_0 satisfies:

$$(\omega-\omega_0)=|(\omega-\omega_0)|e^{-(\alpha+\pi)i/2} . \quad (1.31)$$

In this path, after a variable change $(\omega_1-\omega_{10})^2=a_2(\omega-\omega_0)^2$, the integration path is changed back to the real axis.

$$\frac{\phi(\omega_0)e^{x\eta(\omega_0)a_2}}{\sqrt{-xa_2}}\int_{real} e^{-(\omega_1-\omega_{10})^2}d\omega_1 . \quad (1.32)$$

The subscript $real$ indicates the real axis here. After extending the integration to infinity, the final analytic solution is:

$$\int \phi(\omega)e^{x\eta(\omega)}d\omega \approx \phi(\omega_0)e^{x\eta(\omega_0)}\left(\frac{-2\pi}{x\eta''(\omega_0)}\right)^{1/2}, \text{ with } \eta''(\omega_0)=2a_2 . \quad (1.33)$$

Although the derivation is slightly complicated, the resulting formula is simple. We don't even have to explicitly express the path in the complex plane. What we need to do is check the validity of the Taylor expansion and whether the direction of the critical path is close to the steepest descent direction near the saddle points.

CHAPTER II

THE BLB LAW AND THE TRANSMISSION OF ULTRASHORT PULSES IN WATER

A. The Bouguer-Lambert-Beer (BLB) law

The BLB law was first discovered by Pierre Bouguer, when he studied light attenuation through transparent media. It was thought that light attenuation was merely caused by absorption, while it was later found to be caused by both absorption and scattering. In general, the BLB law describes an exponential dependence of the transmission with respect to the path length. The BLB law can be expressed in a differential equation as below:

$$\frac{dI}{dz} = -CI \ . \tag{2.1}$$

In this differential equation, the loss rate of the physical quantity I is proportional to its own intensity. C is usually a positive constant. For a general pulse propagation problem, $C = \alpha + b$, where α is the absorption coefficient, b is the scattering coefficient, and C is usually called the extinction coefficient. Because our discussion focuses on the spectral regime where the scattering effect is much weaker than the absorption effect, in the following we assume C equals α.

Later studies of light propagation based on electromagnetism showed that the exponential extinction of light as a function of propagation distance is only an approximation for the multi-chromatic light source used in earlier experiments. The propagation of the polarized chromatic field $E(z,\omega)$ through an isotropic homogeneous medium in the $z > 0$ half space according to the introduction in Chapter I follows:

$$E(z,\omega) = \tilde{f}(\omega)\exp[(k(\omega)z - \omega t)i]. \tag{2.2}$$

Recalling that $k(\omega) = \frac{n(\omega)\omega}{c}$, the field in the spectral space can also be written as:

$$E(z,\omega) = \tilde{f}(\omega)\exp[-\omega\,\mathrm{Im}(n(\omega))z/c + i\omega(\mathrm{Re}(n(\omega)z/c - t)]. \tag{2.3}$$

$\tilde{f}(\omega)$ is the Fourier component of the launched pulse. The intensity follows:

$$I(z,\omega) = E(z,\omega)E^*(z,\omega) = F(\omega)\exp(-2\omega\,\mathrm{Im}(n(\omega))z/c), \tag{2.4}$$

where $F(\omega) = \tilde{f}(\omega)\tilde{f}^*(\omega)$ and the corresponding absorption coefficient is

$$\alpha(\omega) = 2\omega\,\mathrm{Im}(n(\omega))/c.$$

The traditional BLB law for the exponential attenuation is only true for monochromatic light. The absorption coefficient $a(\omega)$ is a function of frequency, and therefore the BLB law for each frequency ω is:

$$\frac{dI}{dz} = -\alpha(\omega)I. \tag{2.5}$$

Thus the solution for the transmission of each frequency component is:

$$I(z,\omega) = F(\omega)\exp(-\alpha(\omega)z). \tag{2.6}$$

Our laser source works in a linear regime and the superposition method is applied to obtain the total transmission:

$$T(z) = \int F(\omega)\exp(-\alpha(\omega)z)d\omega. \tag{2.7}$$

Therefore, for non-monochromatic light, especially a pulse with a broad spectrum and steep absorption coefficient distribution, the transmission doesn't attenuate simply exponentially. Here we use a broad conception of BLB law, which includes exponential attenuation for monochromatic light and sub-exponential attenuation for the broad-spectrum light propagation.

B. Simulation of the propagation of ultrashort pulses

One main goal of our experiments is to test the validity of the BLB law. Based on Eq. (2.6) and Eq. (2.7), several inferences can be made:

(1) The transmission at a certain propagation distance only depends on the initial spectrum and the absorption coefficient. Chirps used to modify the phases of pulses only change the temporal properties of the pulses and do not change the spectral intensity. Therefore, chirps don't influence the law of transmission.

(2) The average absorption coefficient $\bar{\alpha}$ (defined as Eq. (2.8)) is a monotonically decreasing function of z, and is always no less than the minimum absorption coefficient $\alpha_{\min}$ in the efficient spectral regime.

$$\begin{aligned}\bar{\alpha} &= \int F(\omega)a(\omega)\exp(-a(\omega)z)d\omega \,/\, \int F(\omega)\exp(-a(\omega)z)d\omega \\ &\geq \int F(\omega)a_{\min}\exp(-a(\omega)z)d\omega \,/\, \int F(\omega)\exp(-a(\omega)z)d\omega \\ &= \alpha_{\min}.\end{aligned} \tag{2.8}$$

Greater absorption coefficients correspond to a faster attenuation. Thus the spectral components of smaller absorption coefficients become more competitive through propagation. The frequency corresponding to the peak of the spectrum is determined by the competition between the initial spectrum and the absorption coefficient distribution at

a certain propagation distance. When z goes to infinity, the remaining frequency component corresponds to the smallest absorption coefficient.

Since the intensity and the power attenuate very quickly, we use a log scale coordinate to describe the transmission. Following Eq. (2.7), the transmission of the power is not an exponential function and the average coefficient $\bar{\alpha}$ describes the average attenuation speed of the overall power.

Our experimental measurement of radiance is a function relating to wavelength, and it is convenient to calculate the transmitted power in wavelength space. For example, Eq. (2.8) can be written as:

$$T(z) = \int g(\lambda)\exp(-a(\lambda)z)d\lambda, \tag{2.9}$$

with $g(\lambda) = 2\pi cF(2\pi c/\lambda)/\lambda^2$.

Predictions and analyses are made for a Gaussian profile pulse propagating in water with different spectral widths and central wavelengths. The predicted spectrum attenuation for a Gaussian profile pulse centered at 800 nm and with a spectral width of 90 nm is shown in Fig. 2.1. As the pulse propagates, the peak slowly moves to the spectral regime with smaller absorption coefficients.

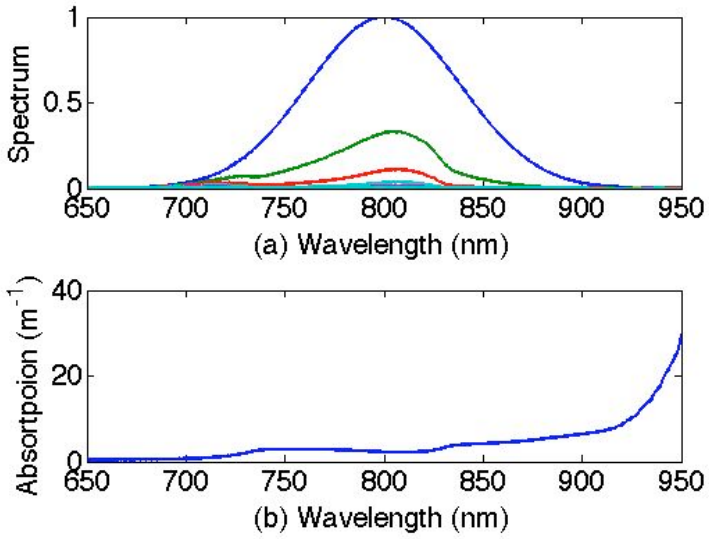

Fig. 2.1 (color online) Spectral attenuation and absorption coefficient. (a) Spectral attenuation for different propagation distances in water from 0 to 5m, and data is obtained for an increase step of 0.5 m from the top to bottom. The pulse is a Gaussian profile with a spectral width 90 nm and is centered at 800 nm. (b) Absorption coefficient of water [21, 22].

The propagation of pulses with two different spectral widths of 45 nm and 90 nm and with four distinctive central wavelengths from 760 nm to 860 nm are simulated. A combination of Pope and Kou's data is used in the simulation [21, 22]. The attenuation of broader spectrum pulses is generally slower than the narrower ones as shown in Fig 2.2 (a), while the rate of decrease of the average absorption coefficients are greater than the narrower counterpart in Fig 2.2 (b). For pulses with same spectral width but at different spectral regime (different central wavelengths), the greater absorption coefficients in the longer wavelength regime cause much lower energy at even a small propagation distance.

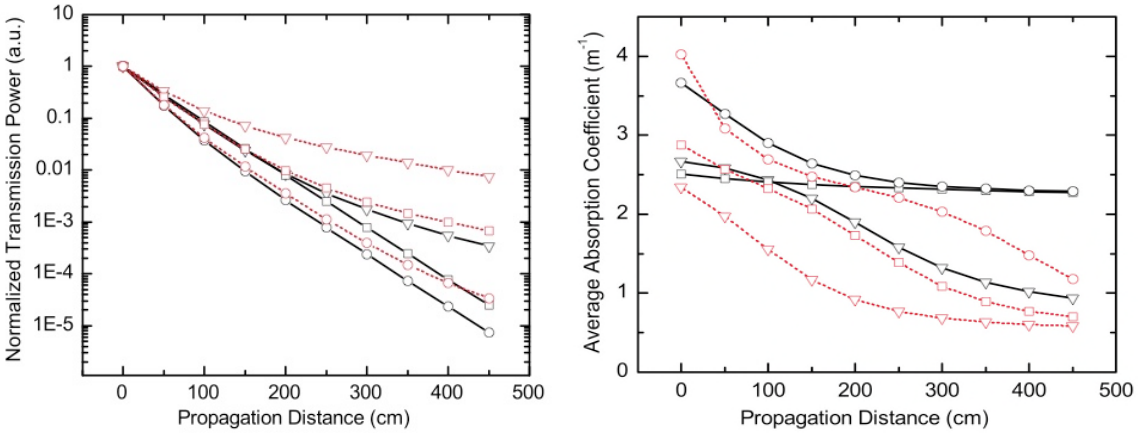

(a) Power transmission (b) Average absorption coefficient

Fig. 2.2 (color online) Pulse transmission in water. The circles, squares, and triangles denote center wavelengths of 760,800 and 840 nm and the solid and dashed lines denote bandwidths of 45 and 90 nm. (a) Simulation of power transmission as a function of propagation distance. (b) Simulation of the average absorption coefficient as a function of propagation distance.

C. Experimental results

In our experiment with setup shown in Fig. 2.3 [23], we employed a Ti: sapphire-based laser system, consisting of an oscillator (Mira, Coherent: 800 nm center wavelength, 80 nm FWHM band-width, 500 mW average power, 76 MHz repetition rate) and an amplifier (Legend; Coherent: 35 fs pulse duration, 1kHz repetition rate, 1mJ pulse energy). The parameters of the laser were chosen to best match with earlier experiments [9-13]. One of the key factors in our experiment was to exclude any nonlinear effect. The pulses are attenuated by the neutral density filters and passed through a telescope to reduce the beam size before entering the water sample (see Fig 2.4). The beam size is approximately 10 mm for the amplified beam and 2 mm for the oscillator beam. The water sample is contained in a cylindrical glass cell whose length can be varied from 150 to 450 cm. The output signal is measured first by a power meter (1815-C, Newport) and

then by a spectrometer (USB2000, Ocean Optics) after reflected off a speaker, which is applied to eliminate pulse speckles.

We take special care to establish that each experiment is completed within the linear regime of the response of the medium. We vary the input power using the neutral density filter, and measure the output, and establish a linear regime for input power below 8.6 mW, where the transmitted power is a linear function of the input power as shown in Fig 2.4. The power we used in experiments is within this range. We design the experiments with varying parameters of pulse duration, repetition rate and chirps. First, we vary the pulse chirp (and therefore its duration) while keeping the spectrum the same. Then, we increase the pulse duration by cutting the spectrum.

The total transmitted power is measured by the power meter and is also calculated by integration of the spectrum measured by the spectrometer. Comparison between simulation experimental results is made in Fig. 2.5 and Fig. 2.6 to verify that the attenuation behavior is consistent with the BLB law. We have to point out as we mention above, the transmission is only a sub-exponential and thus not straight line in a semi log coordinate. The seeming linear behavior in our figure is because the relatively narrow spectral width of the pulse and the absorption coefficient is a relatively flat and symmetric function of frequencies in this regime.

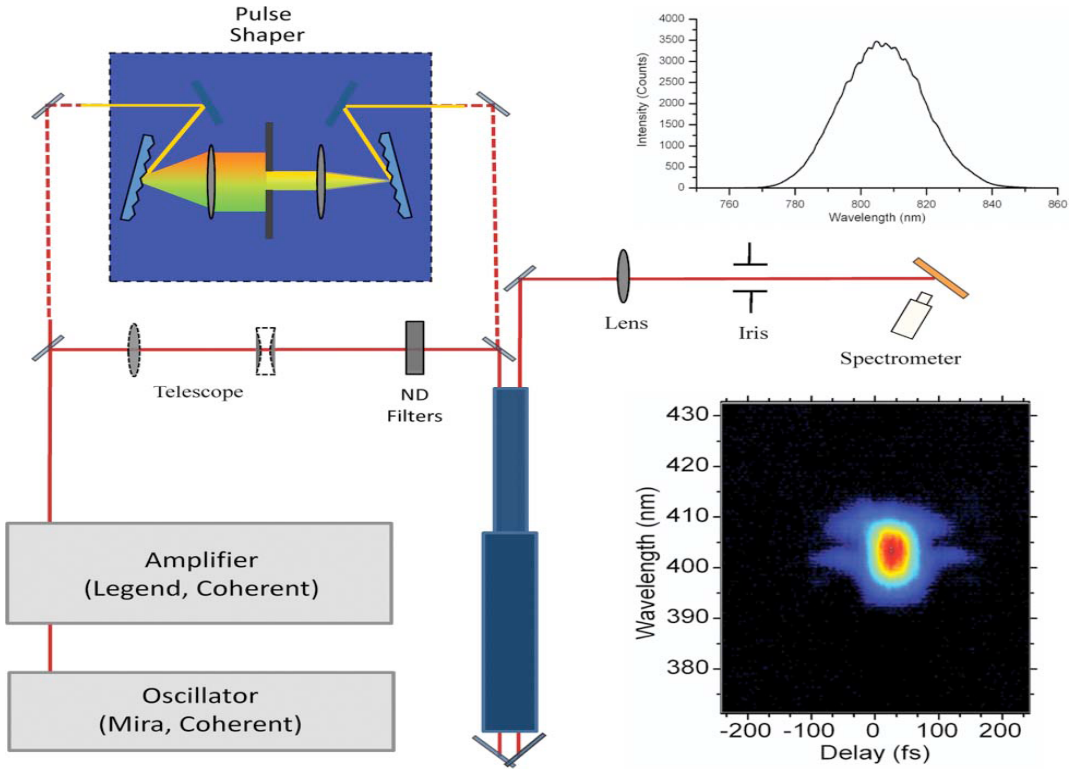

Fig. 2.3 (Color online) Experimental setup. The beam path through the amplifier, pulse shaper, and telescope is optional, depending on the experiment performed. The upper right inset shows the input pulse spectrum, while the lower right inset shows a frequency-resolved optical gating trace of the transform-limited input pulse. ND, neutral density.

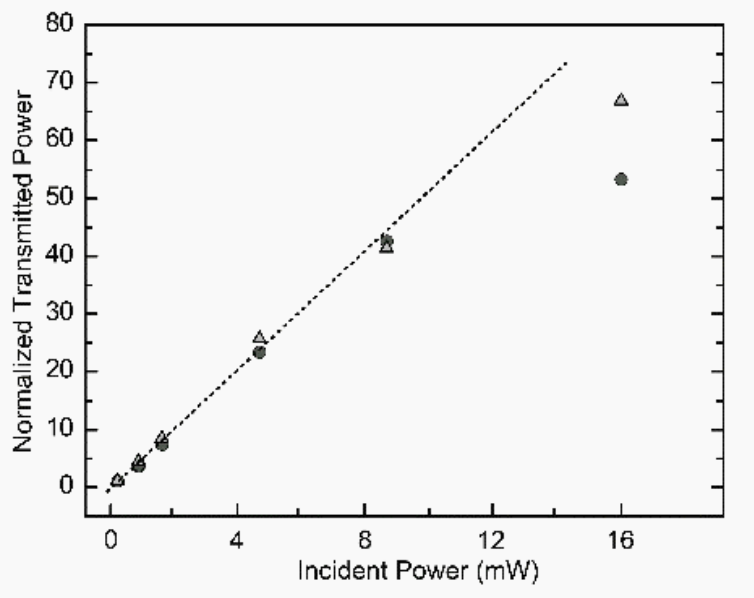

Fig. 2.4 (Color online) Normalized transmitted power for amplified pulses propagating through 150 cm of water as a function of incident power. The triangles designate power meter measurements, while the circles designate integrated spectrometer measurements. The dashed line represents the expected trend for linear behavior. It can be seen that for total incident powers above 8.6 mW, the transmitted power deviates from linear behavior. Therefore, all experiments are conducted at incident power levels at or below this point. All error bars are smaller than the size of the symbols.

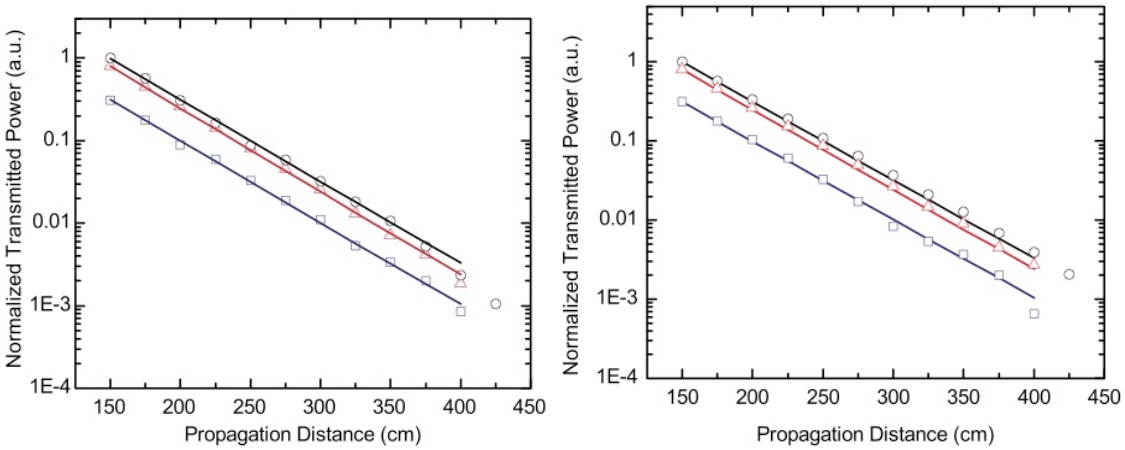

(a) Power measured by the power meter. (b) Power measured by the spectrometer

Fig 2.5 (Color online) Total measured power as a function of propagation distance. The circles and squares represent amplified pulses with total incident powers of 8.6 and 4.8 mW, respectively. The triangles represent oscillator pulses with total incident power of 43 mW; solid lines indicate the predicted simulated behavior for each pulse following Eq. (2.7). All error bars are smaller than the size of the symbols. (a) Power measured by the power meter. (b) Power measured by the spectrometer.

Our spectrometer enables us to analyze the transmission for single frequency components, which provides a direct way to verify the BLB law. The attenuation for several frequencies is shown in Fig. 2.6. By linear regression, we can obtain the absorption coefficients from the experimental data and the results agree very well with the existed absorption data obtained by Kou [21] as shown in Fig. 2.7. For more absorption data in a short wavelength regime, Pope and Fry's data is also used [22]. It is also found that there are no significant changes in transmitted power when applying chirps to the pulse and changing the pulse duration.

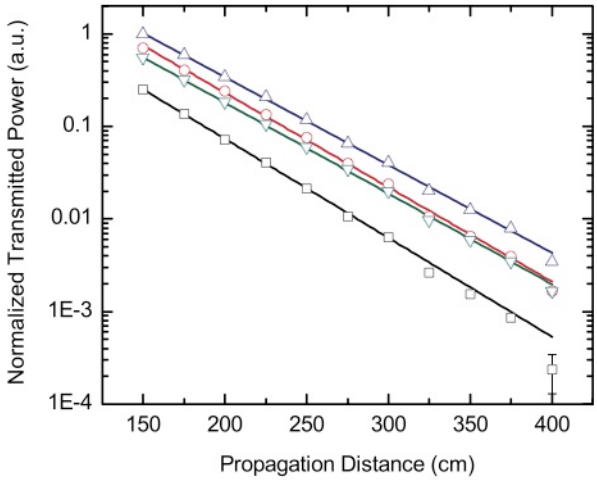

Fig. 2.6 (Color online) Spectral power for various wavelengths as a function of propagation distance. The light source are amplified pulses with total incident power of 4.8mW. Squares, circles, and triangles with apices up and sown represent wavelengths of 700, 800, 810 and 820 nm, respectively. The solid lines are exponential fits weighted with uncertainty. All error bars not shown are smaller than the size of the symbols.

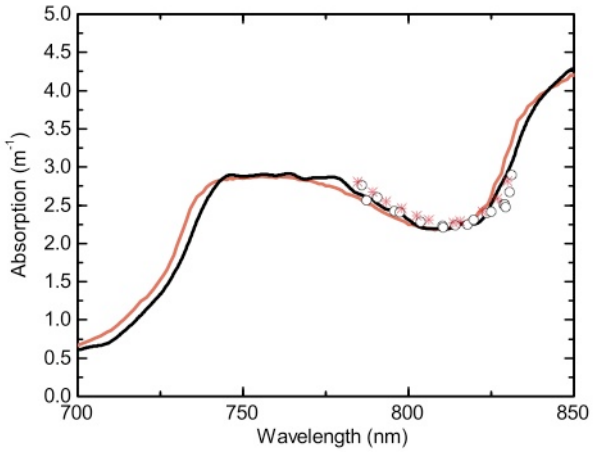

Fig. 2.7 (Color online) Comparison of absorption curves of water. The data groups are measured by Kou et al. [21] (lighter curve), and measured from the deionized water sample. Also shown are absorption coefficients measured by laser oscillator (asterisks) and amplified pulses (circles) with total incident powers of 43 and 4.8 mW, respectively.

D. Conclusion and discussion

Though the bandwidth of the spectrum influences the attenuation of the power, it still falls into the category of the BLB law by a superposition of exponential attenuation. Our results are inconsistent with the claims that the propagation of ultrashort pulses violates the BLB law. However, we are still not able to make a conclusion about whether there is any precursor existed in the experiments. This question would be answered in the following chapters.

A transmission-limited ultrashort pulse has a very broad spectrum and thus large dispersion. Therefore any device, even a very thin optical device can apply dispersion to the pulse and increase the pulse duration. For example, the tank, which contains the water cell, has a glass window. To compensate for the dispersion caused by the glass window, a sophisticated autocorrelator must be used to monitor the pulse duration while Dazzler is used to compensate for this dispersion. As an example, we compared pulse widening of an initially 30 fs and 7 fs pulse, both of which we employed in our experiment. For the convenience of comparison, we use Gaussian profiles and the same central wavelength for both pulses and we found that through a glass with a thickness less than 2 mm, the pulse duration of initial 7 fs pulse becomes even longer than the initial 30 fs one as shown in Fig. 2.8.

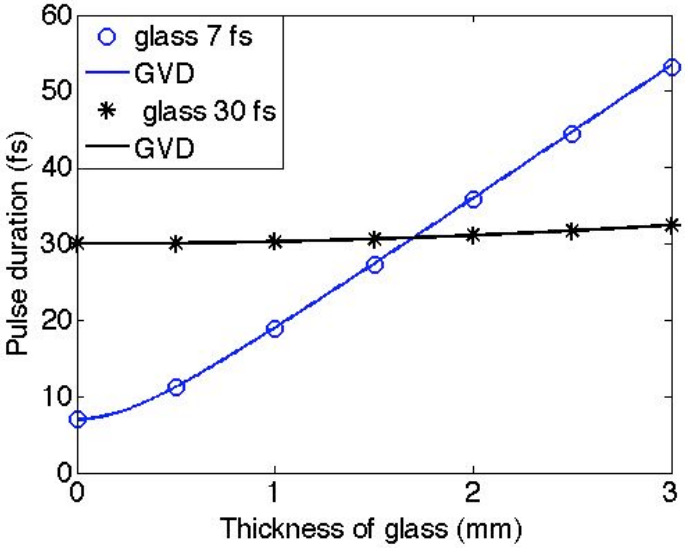

Fig. 2.8 (color online) Comparison of pulse durations through glass. Incident 7 fs and 30 fs pulses centered at 800 nm are employed. GVD is the group velocity dispersion (see Chapter IV for details). Circles and stars represent pulse durations calculated by the actual refractive index while the solid lines represent the results calculated by the GVD (or linear dispersion) approximation. The refractive index of the BK 7 glass is determined by the Sellmeier equation [24].

CHAPTER III

APPLYING THE SADDLE POINT METHOD TO PULSE PROPAGATION IN A LORENTZ MEDIUM

A. Dynamics of the electric field propagation in a Lorentz medium

In Chapter I, we introduced the saddle point method. In this chapter, we apply this method to solve the pulse propagation problem in a Lorentz medium. In the simulation, symbols and parameters of the Lorentz medium and the initial spectrum follow Oughstun's paper [25]. A pulse is launched at the interface between vacuum and the Lorentz medium located in the $z > 0$ half space. The pulse is polarized and propagates in the positive z direction and thus it is a one-dimensional pulse propagation problem. The electric field can be expressed as (see Chapter I):

$$E(z,t) = \frac{1}{2\pi}\mathrm{Re}\int_{-\infty}^{\infty} u(\omega-\omega_c)e^{i(k(\omega)z-\omega t)}d\omega, \text{ with } k(\omega) = \frac{n(\omega)\omega}{c}. \qquad (3.1)$$

$E(z,t)$ is the electric field as a function of time and propagation distance and $u(\omega-\omega_c)$ is the initial spectral amplitude , which can be obtained from the Fourier transformation of the launched pulse at $z = 0$:

$$u(\omega-\omega_c) = E(0,\omega) = \frac{1}{\sqrt{2\pi}}\int_{-\infty}^{\infty} E(0,t)e^{-i\omega t}dt, \qquad (3.2)$$

$$\text{with } E(0,t) = f(t) = \exp[-(\frac{t-t_0}{T})^2]\sin(\omega_c t+\psi), \qquad (3.3)$$

where ω_c is the carrier frequency, ψ is the initial phase of the signal, t_0 is the time corresponding to the pulse peak, and T is a time parameter which is proportional to the

pulse duration. For simplicity and with no loss of generality, we assume $t_0 = 0$, $\psi = 0$. Following Eq. (3.2),

$$u(\omega - \omega_c) = \pi^{1/2} T \exp[-a(\omega - \omega_c)^2] = u_0 \exp[-a(\omega - \omega_c)^2]. \tag{3.4}$$

Define $u_0 = \pi^{1/2} T$ here. In the simulation, following Oughstun [25], define zd as the distance of the 1/e attenuation of the field amplitude at the carrier frequency ω_c or $zd = \dfrac{c}{\mathrm{Im}(n(\omega_c)\omega_c}$. Define the generalized dimensionless space-time parameter $\theta = c(t - t_0)/z$ and thus the phase can be written as a form of $\dfrac{z\Phi(\omega,\theta)}{c}$, with

$$\Phi(\omega,\theta) = i\omega[n(\omega) - \theta] - a(\omega - \omega_c)^2 c/z. \tag{3.5}$$

The values of the parameters are:

$2T = 2.0 \times 10^{-16}$ sec,

$\omega_c = 5.75 \times 10^{16}$ sec^{-1},

$\omega_0 = 4 \times 10^{16}$ sec^{-1},

$b^2 = 20 \times 10^{32}$ sec^{-2},

$\delta = 0.28 \times 10^{16}$ sec^{-1}.

The linear dielectric is described by the single resonance Lorentz model, and the refractive index follows:

$$n(\omega) = (1 - \frac{b^2}{\omega^2 - {\omega_0}^2 + 2i\delta\omega})^{1/2}, \tag{3.6}$$

where ω_0 is the undamped resonance frequency, b is the plasma frequency and δ is the damping constant of the lossy dielectric. A Lorentz medium has a very sharp absorption peak near the resonance frequency as shown in Fig. 3.1.

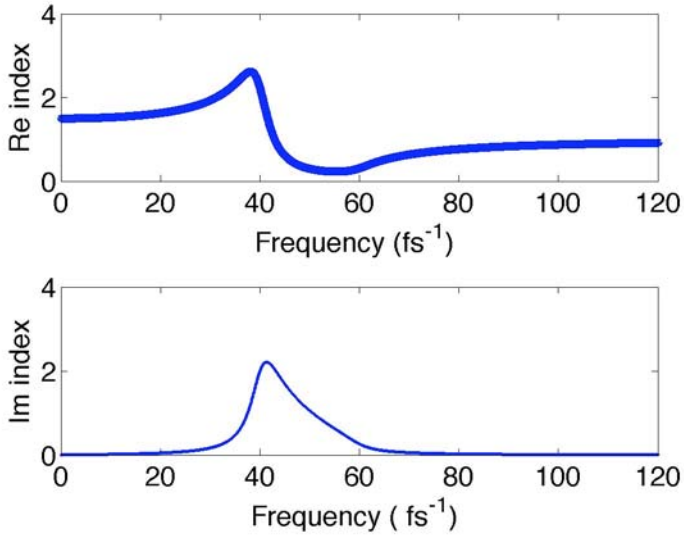

Fig. 3.1 (color online) Real part and imaginary part of the refractive index of a Lorentz medium. The parameters are chosen the same as those in the simulation.

Before applying the saddle point method, comparing the expression in Eq. (3.1) and Eq. (1.27), $\phi(\omega)=1$, x is replaced by z/c and $\eta(\omega)$ is replaced by Eq. (3.7).

$$\eta(\omega)=\Phi(\omega,\theta)=i\omega(n(\omega)-\theta)-a(\omega-\omega_c)^2 c/z\text{, with }\theta=ct/z. \tag{3.7}$$

For a more general function $u(\omega-\omega_c)$, we can write $\eta(\omega)$ as:

$$\eta(\omega)=i\omega(n(\omega)-\theta)-ln(u(\omega-\omega_c))c/z. \tag{3.8}$$

When including the detailed form of the spectrum, the electric field can be explicitly expressed as:

$$E(z,t)=\frac{1}{2\pi}\mathrm{Re}(\int_{-\infty}^{\infty} e^{z/c[i\omega(n(\omega)-\theta)-a(\omega-\omega_c)^2 c/z]}d\omega). \tag{3.9}$$

By this comparison, the saddle points are determined by the following equation:

$$\frac{d\Phi(\omega,\theta)}{d\omega}=i(n(\omega)-\theta)-i\omega\frac{dn(\omega)}{d\omega}-2a(\omega-\omega_c)c/z=0. \tag{3.10}$$

The equation generally has five solutions for the Lorentz medium and so there are five saddle points. The five saddle points change as θ changes and have a trajectory as shown in Fig. 3.2. The saddle points are named according to the magnitudes their real part. For example, saddle point 1 (sp 1) is the saddle point with the smallest real part while saddle point 5 (sp 5) is the saddle point with the greatest real part.

We construct a path in the complex plane which passes along or close to the direction of steepest descent, and the path includes the saddle points near the real axis while excludes the saddle points with large imaginary values. As shown in Fig. 3.3 (a), the green saddle point is in the deformed path while the red one is not. For a later time, if the originally more distant saddle point comes closer to the real axis, we should change the path to pass both of the saddle points (the dashed pink line in Fig. 3.3 (b)).

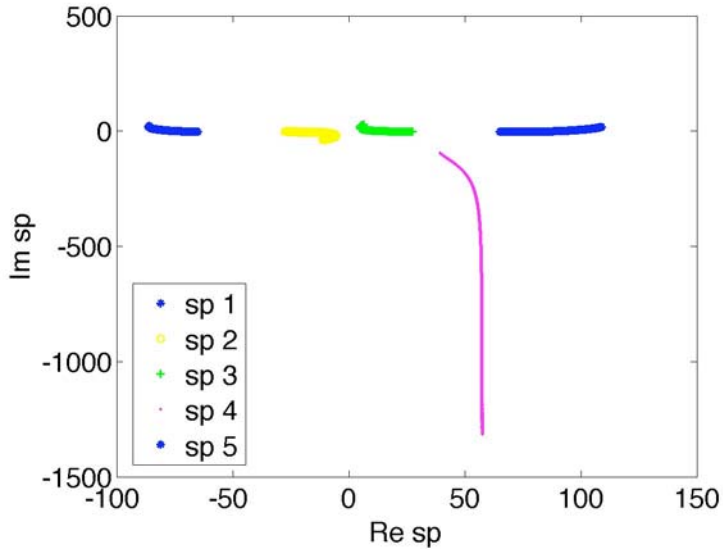

(a)

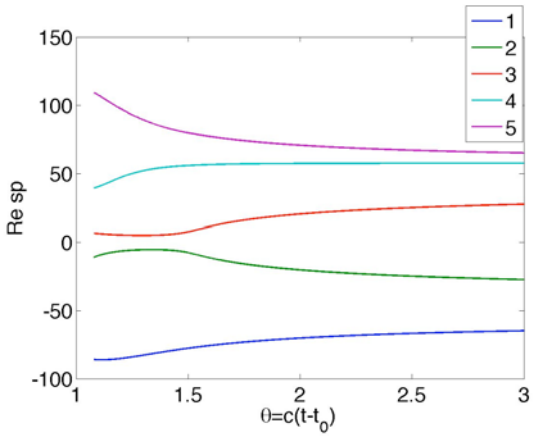

(b)

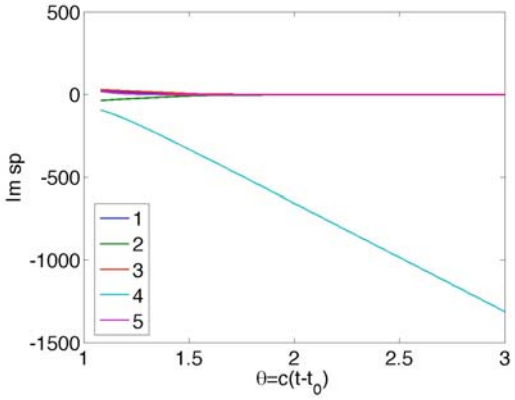

(c)

Fig. 3.2 (color online) Five branches of saddle points for $z/zd = 82.64$. (a) The trajectory of the five saddle points in the complex plane. (b) The real part of the saddle points change as a function of θ. (c) The imaginary part of the saddle points change as a function of θ.

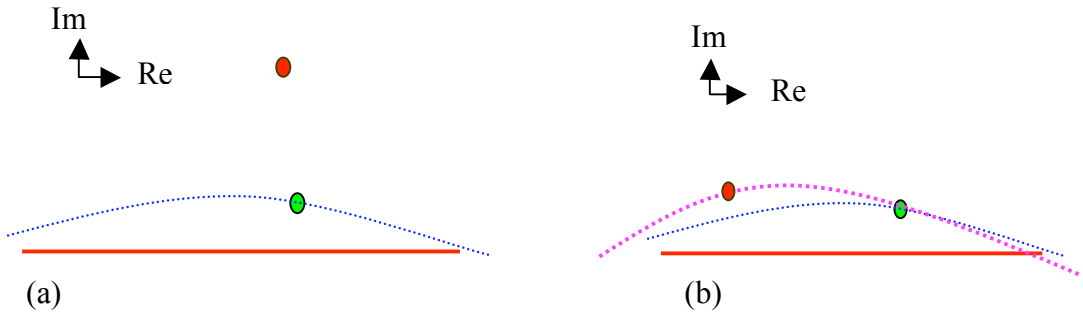

Fig 3.3 (color online) Graph description of the deformed path passing saddle points. The red line is the real axis. Two small circles represent saddle points. (a) The red saddle point is distant from the real axis and it is not included in the path (the dashed blue line). (b) As θ becomes larger, the red saddle point gets closer to the real axis, and it begins to contribute to the integration since it is now close to the path and the path should be changed to pass both of the saddle points as the dashed pink line.

Simulation results by the saddle point method compared with the electric field obtained by direct integration are shown in Fig. 3.4 and Fig. 3.5 for different propagation distances from $z/zd = 20.66$ to $z/zd = 300$. We analyzed a little more detail about the so-called generalized Sommerfeld and Brillouin precursor as stated by Oughstun [25], at $z/zd = 82.64$.

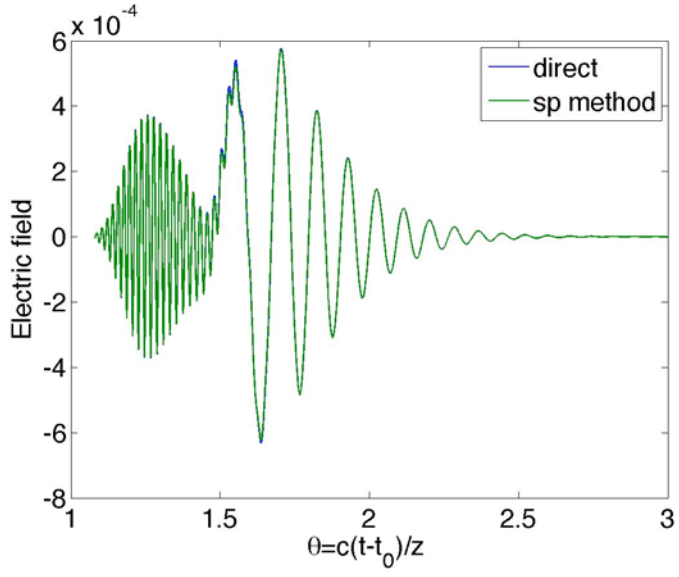

(a)

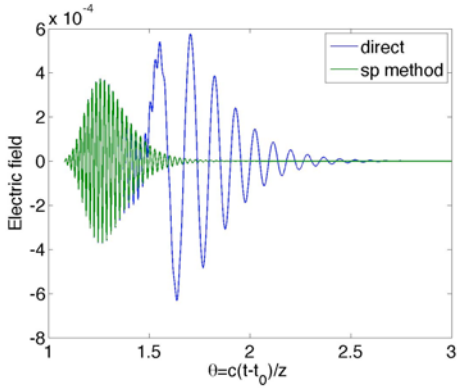

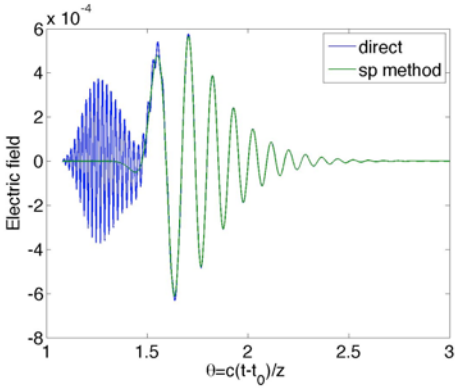

(b) (c)

Fig. 3.4 (color online) Comparison of electric field by direct integration method and the saddle point method at $z / zd = 82.64$. The blue line represents the result achieved by the direct integration and the green line by the saddle point method. (a) The green line is mainly contributed to by saddle point 3 and saddle point 5 in Fig. 3.2, corresponding the generalized Brillouin and Sommerfield precursor, respectively. (b) The green line is contributed to by saddle point 5 and it matches with the field by direct integration in the high frequency component. (c) The green line is contributed to by saddle point 3 and it matches with the field by direct integration in the low frequency component.

There are both Sommerfeld and Brillouin precursors; the Sommerfeld precursor (high frequency) is due to the contribution of the path near saddle point 5 while the

Brillouin precursor (low frequency) is due to the contribution of the path near saddle point 3. The saddle point method not only gives an approximation with great accuracy but also provides separate saddle points to represent the Sommerfeld and Brillouin precursors in a straightforward way. More simulation results are shown in Fig. 3.5.

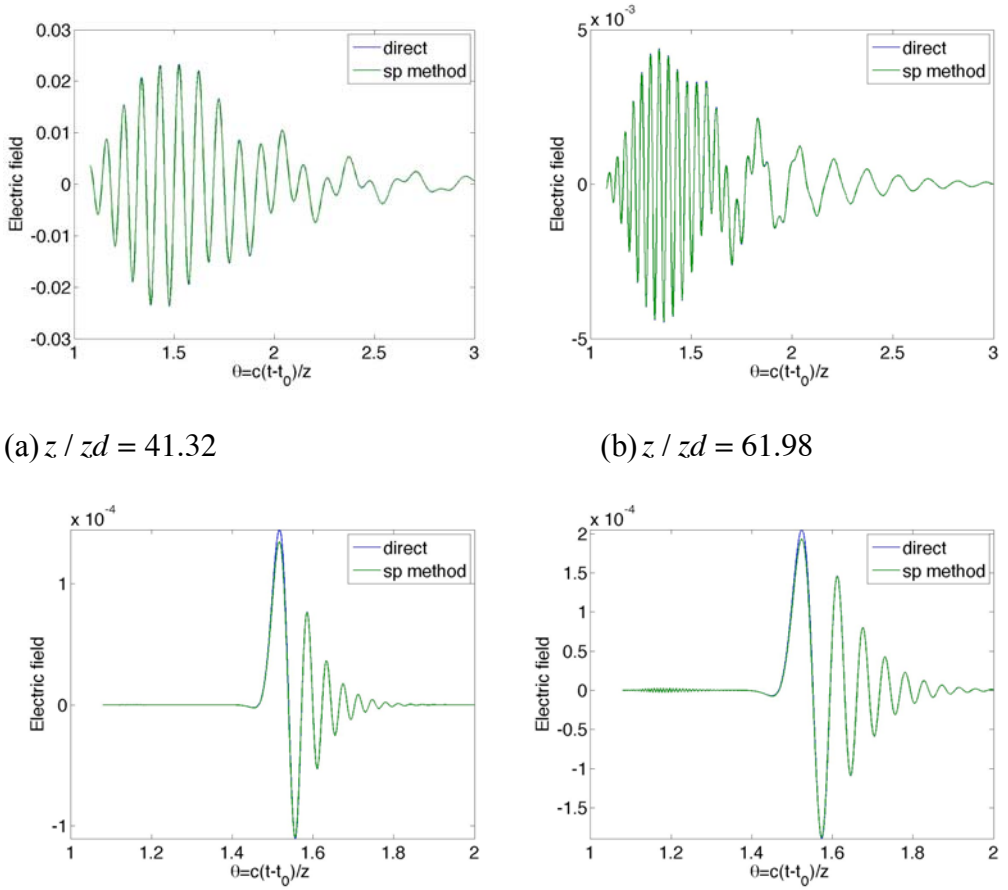

(a) $z / zd = 41.32$ (b) $z / zd = 61.98$

(c) $z / zd = 200$ (d) $z / zd = 300$

Fig. 3.5 (color online) Comparison of electric field by direct integration method and the saddle point method at different propagation distances. The range is from $z / zd = 20.66$ to $z / zd = 300$.

When z increases to 300 zd, only one pattern of the electric field is visible, which is mainly contributed by saddle point 3, which means that the Sommerfeld field has died out and only the Brillouin field exists.

From the principle of asymptotic expansion, the saddle point method should be more accurate for greater z. Up to the maximum z in our simulation, the match between the direct integration of electric field and saddle point method is all right, we can still see apparent deviation around $\theta = 1.55$ in Fig. 3.5 (c) and (d). The reason may lie in that the truncation of the Taylor expansion of the phase to second order is not valid because the value of the second order coefficient is too small. To further justify this point, the value of the second order coefficient as a function of θ at the saddle point in the Taylor expansion are shown in Fig. 3.6, which have a minimum around $\theta = 1.55$ (see Eq. (1.29)). One possible way to solve this deviation is to keep more terms in the expansion but the result is no longer analytic.

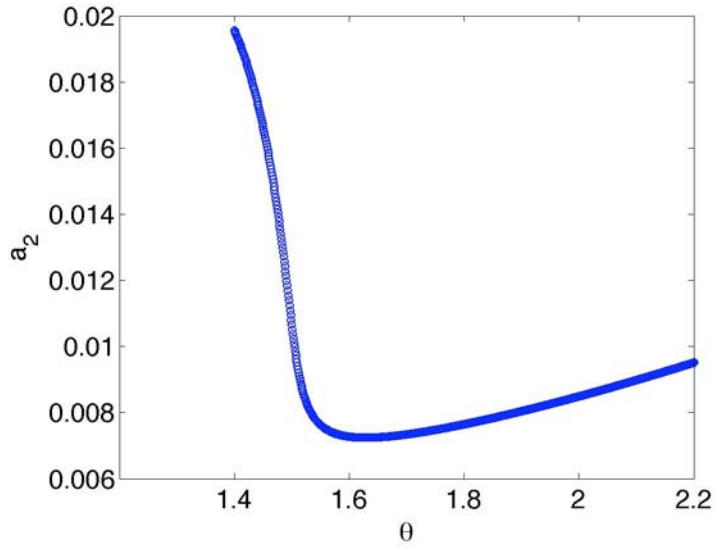

Fig. 3.6 The value of the second order coefficient a_2 in the Taylor expansion of Eq. (1.29) as a function of θ.

B. Exponential attenuation of the electric field and the spectral attenuation

There is still a very important unanswered question: whether light attenuation can be less than exponential, for example, algebraic. Österberg [9] claimed for some special θ (or time), the real part of the coefficient in front of z becomes zero in the phase (Eq. (3.12)) and the field has no exponential but only algebraic dependence on the propagation distance. As to the practical application, the question is: does this phenomenon happen for a dominant θ, or whether a significant part of the energy decays algebraically. One reason to reject this point is from the viewpoint of transmission. The intensity for monochromatic light follows the BLB Law and the total intensity is a sum of exponential functions (still much faster than algebraic decay). Another way is to examine the field attenuation in time domain directly. The electric field obtained by the saddle point method has an analytic expression from Eq. (1.33):

$$A(z,t)=\sum_{j=1}^{k}A_j(z,t)\,. \tag{3.11}$$

$$A_j(z,t)=(\frac{c}{2\pi z})^{1/2}\,\mathrm{Re}[\frac{1}{(-\Phi^{"}(\omega_{sp_j},\theta))^{1/2}}\exp(\frac{z}{c}\Phi(\omega_{sp_j},\theta))]\,. \tag{3.12}$$

$A(z,t)$ is the electric field contributed by all the saddle points, while $A_j(z,t)$ is the electric field given by the j_{th} saddle point ω_{sp_j}.

For z>200 zd, only one saddle point significantly contributes to the field. For different z ranging from 200 zd to 400 zd, the amplitude of electric field is shown in Fig. 3.7.

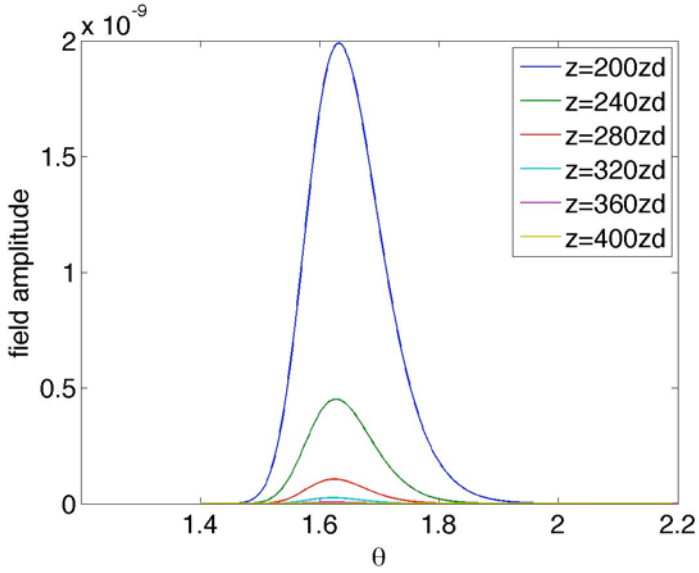

Fig. 3.7 (color online) Amplitude of the electric field as a function of θ for different propagation distances. The lines from top (blue color) to bottom (yellow color) represent different z ranging from 200 zd to 400 zd.

If we fix the value of θ, the attenuation approximately follows the BLB law as shown in Fig. 3.8.

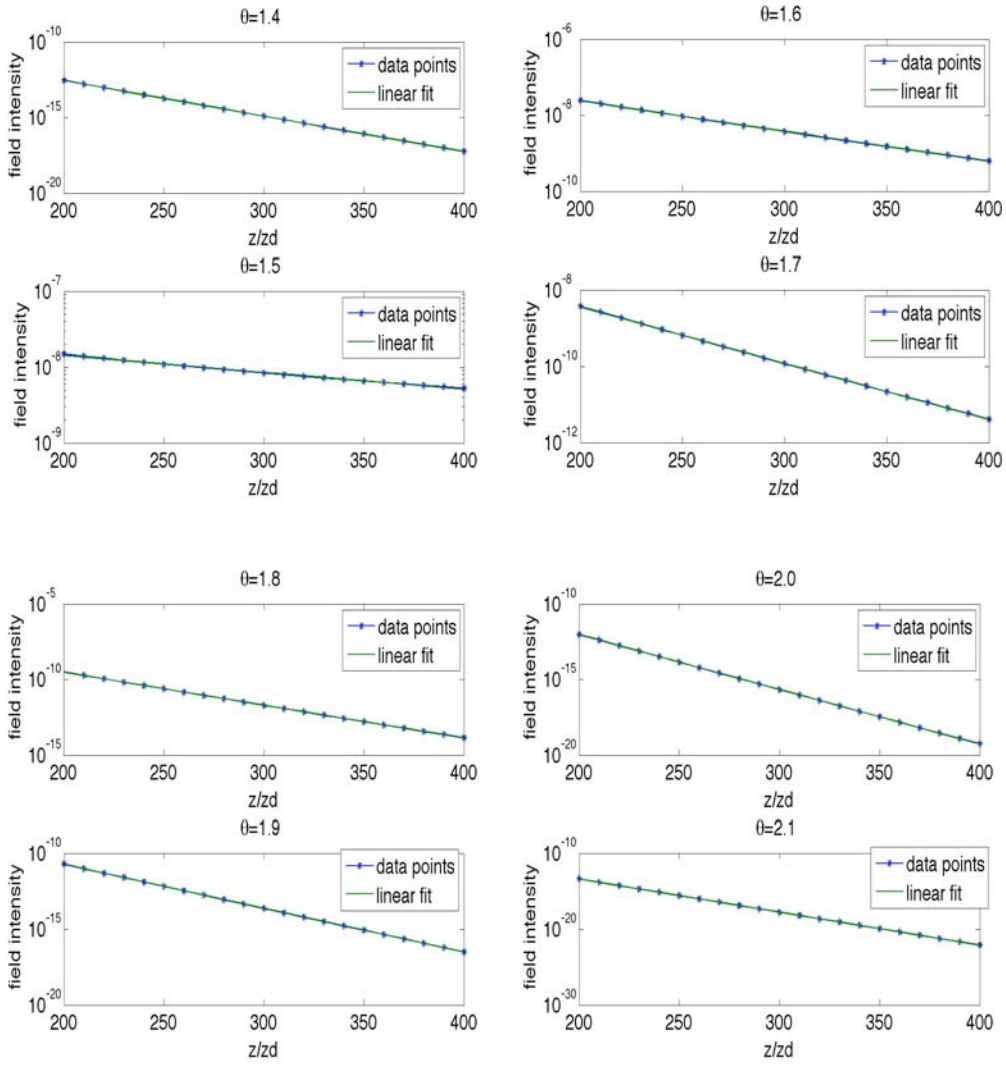

Fig. 3.8 (color online) The intensity of electric field as a function of propagation distance for different θ ranging from 1.4 to 2.1. The axis of y is a log scale. The blue dots represent the intensity for a certain θ and the green line is the linear fit.

We can derive a similar formula as the BLB law in the time domain. The total energy of the electric field is:

$$
\begin{aligned}
I(z) &= \int_{-\infty}^{\infty} \left(A_j(z,t) A_j(z,t)^* \right) dt \\
&= z/c \int_{-\infty}^{\infty} \left(A_j(z,t) A_j(z,t)^* \right) d\theta \\
&= \int_{-\infty}^{\infty} \frac{1}{2\pi abs(\Phi''(\omega_{sp},\theta))} e^{-2\frac{z}{c}\mathrm{Im}\,\omega_{sp}[n(\omega_{sp})-\theta]} d\theta.
\end{aligned}
\tag{3.13}
$$

By comparison to the actual BLB law, $\frac{1}{2\pi abs(\Phi''(\omega_{sp},\theta))}$ is the spectral intensity with respect to θ and $n(\omega_{sp})-\theta$ is the corresponding refractive index as a function of θ.

The absorption properties separate the spectrum into two parts as the pulse passes through the medium as shown in Fig. 3.9 (a-c). At first, the high frequencies dominate and the Sommerfeld precursor develops. As z increases, the low frequency spectral components become more important, and thus the energy gradually concentrates in the Brillouin precursors.

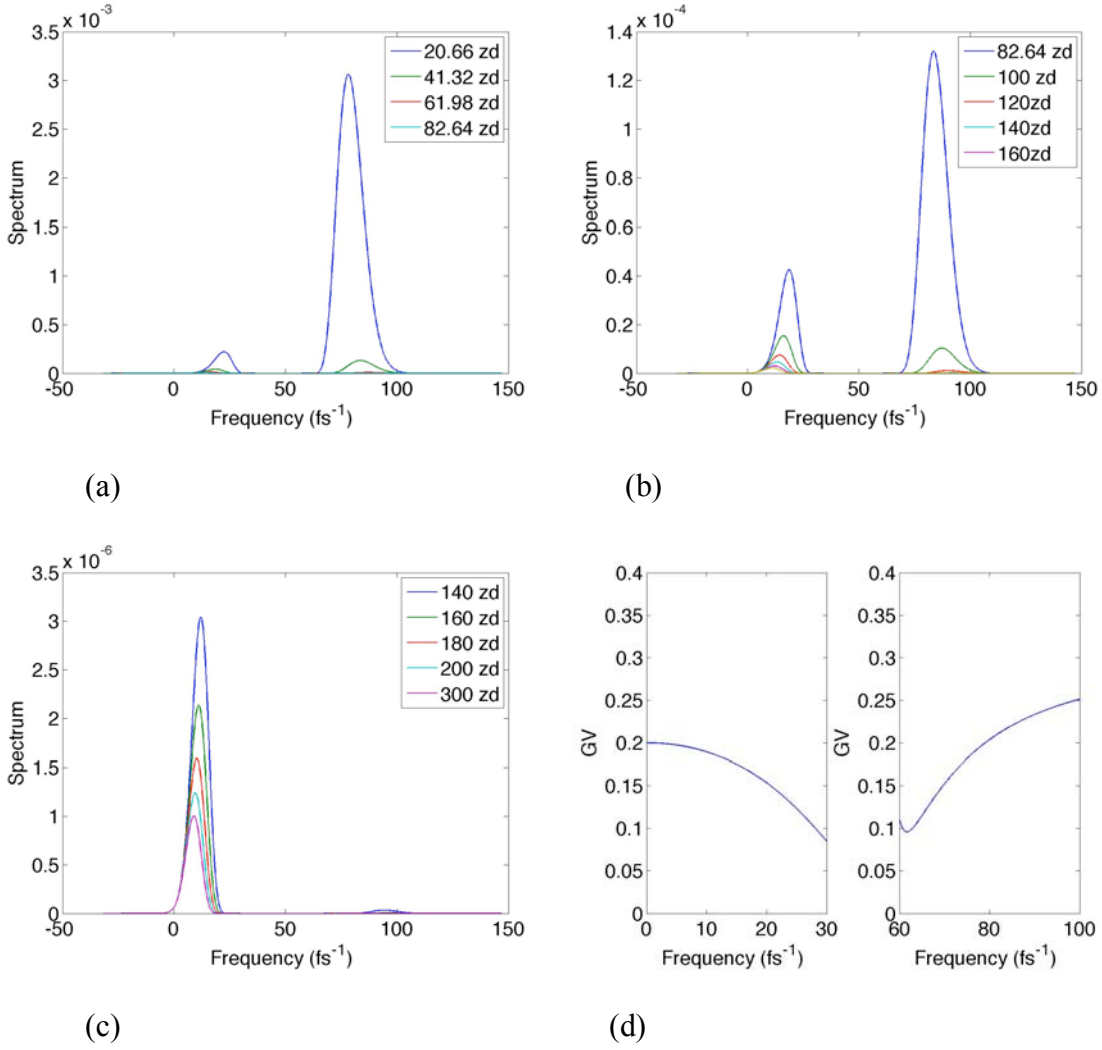

Fig. 3.9 (color online) Spectral attenuation and group velocity. (a) Spectrum at propagation distances from $z/zd = 20.66$ to $z/zd = 82.64$ when the Sommerfeld precursor dominates. (b) Spectrum at propagation distances from $z/zd = 82.64$ to $z/zd = 120$, when Sommerfeld and Brillouin precursor coexist. (c) Spectrum at propagation distance greater than $z/zd = 140$, when only Brillouin precursor dominates. (d) Group velocity (GV) for the two ranges of frequency 0-30 fs^{-1} and 60-100 fs^{-1}, respectively.

We here make a comment that the study of precursors or forerunners in Brillouin's book emphasized the wave front of the pulse (when θ is close to 1). While in Oughstun's paper and book, the saddle point method in fact is applied to solve for the electric field, which may not be appropriate for the name "precursor". Only the wave front of the Sommerfeld precursor in the high frequency limit can be called a precursor in the traditional meaning. The generalized Sommerfeld precursor comes earlier than the Brillouin precursor because the group velocity as shown in Fig. 3.9 (d) is greater for high frequency components when compared with low frequency components which are determined by the refractive index of the Lorentz medium. Therefore, to observe precursors instead of mere pulse breakers, shorter pulses with a very steep rise, which is similar to the step-modulated signal applied in Brillouin's book, is required.

CHAPTER IV

APPLYING THE SADDLE POINT METHOD TO ULTRASHORT PULSE PRPAGATION IN WATER

A. Dynamics of the electric field propagation in water

The saddle point method has only been applied to a medium with a sharp absorption peak and high dispersion (such as the Lorentz medium) and this method turns out to be a very good approximation. For water, the refractive index is smoother compared to the Lorentz medium and thus has much less dispersion. At first glance, the saddle point method seems not to work well for ultrashort pulse propagation in water. However, it turns out that the results are even better when applied to water than to the Lorentz medium and thus we conclude the saddle point method is a general method to solve pulse propagation problems.

To make the simulation results more relevant to the actual laser, a Gaussian profile pulse centered at 600 nm and with pulse duration of 10 fs is chosen. The analytic refractive index (Eq. (4.1) and Eq. (4.2)) we use here is from Quan and Fry [26] and it matches very well with the measured refractive index data in a range from 200 to 1100 nm as verified in [27]. The spectrum of the pulse for the simulation is shown in Fig. 4.1. Therefore, the analytic fit to the refractive index is sufficient for our simulation.

$$n(\lambda) = 1.31279 + 15.762\lambda^{-1} - 4328\lambda^{-2} + 1.1455\times 10^{6}\lambda^{-3}, \text{ with } \lambda \text{ in nm.} \qquad (4.1)$$

$$n(\omega) = 1.31279 + 8362\times 10^{-6}\omega - 1.21811\times 10^{-3}\omega^{2} + 1.7104810^{-4}\omega^{3},$$

with ω in fs^{-1}. (4.2)

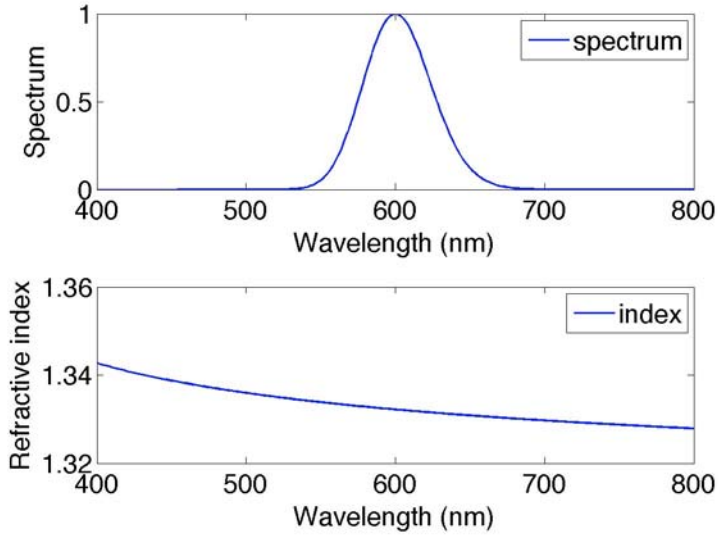

Fig. 4.1 (color online) Spectrum and the refractive index of water used in simulation.

Water absorption is not as significant as dispersion in the spectral regime we consider here (from 400 to 800 nm for example) and the absorption doesn't contribute to the fast phase oscillation, therefore we neglect it here. It is not difficult to add the absorption and this results in a complex index rather than a real index. We extend the frequency regime of the refractive index to infinity. Although, the refractive index doesn't follow Eq. (4.1) outside the range from 200 to 1100 nm, the detailed form of the refractive index doesn't influence the field as long as the spectral intensity is negligible there (due to Gaussian profile distribution of the spectrum).

Following the same process which we applied in Chapter III to a Lorentz medium, we solve pulse propagation in water at propagation distances from 60 μm to 6 m, which corresponds to 10^2 to 10^7 times the carrier wavelength of 600 nm. We use a 10 fs

Gaussian profile pulse as the launched pulse. The initial electric field and the electric field in the spectral space (the spectral amplitude) are:

$$E(0,t) = \frac{1}{\sqrt{2\pi}} \exp(-\frac{2\ln(2)t^2}{\tau_0^2}) \cos(\omega_c t), \tag{4.3}$$

$$u(\omega - \omega_c) = \exp[-\frac{(\omega - \omega_c)^2 \tau_0^2}{8\ln(2)}] = \exp[-a(\omega - \omega_c)^2]. \tag{4.4}$$

Define $a = \frac{\tau_0^2}{8\ln(2)}$. Here in the simulation $\tau_0 = 10\,fs$ is the initial pulse duration, and ω_c is the carrier frequency with a value about 3.14 fs^{-1} as calculated by the central wavelength λ_c (600 nm):

$$\omega_c = \frac{2\pi c}{\lambda_c} = 3.14\,fs^{-1}. \tag{4.5}$$

The saddle points are obtained by solving

$$\frac{d\Phi(\omega,\theta)}{d\omega} = i(n(\omega) - \theta) - i\omega\frac{dn(\omega)}{d\omega} - 2a(\omega - \omega_c)c/z = 0. \tag{4.6}$$

$n(\omega)$ is the analytic refractive index (Eq. (4.2)). There are three saddle points, because Eq. (4.2) is a third order polynomial. The saddle points are ordered according to the magnitudes of their real part. Only the last two saddle points play a role in the integration (Eq. (1.10)). As θ changes, or similarly as time changes, each saddle point has a trajectory in the complex plane. For example, at a propagation distance of 6 cm in water, the trajectory for the three branches of saddle points are shown in Fig. 4.2.

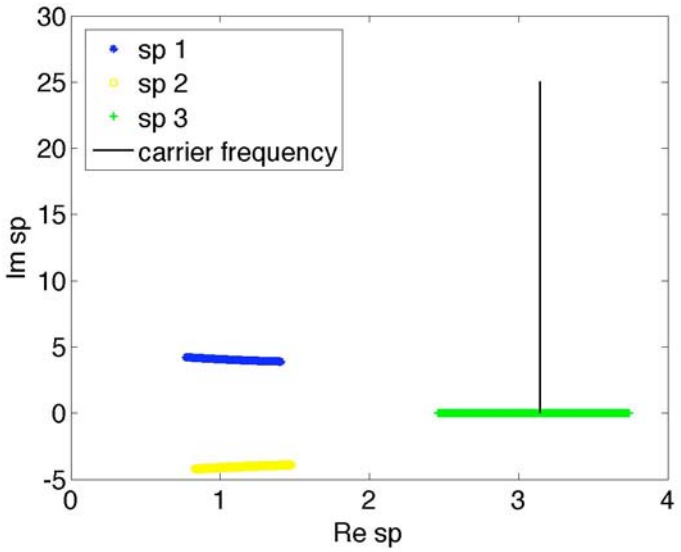

Fig. 4.2 (color online) Saddle point trajectory. For a fixed value of θ, sp 1 represents the saddle point with the smallest real part and sp 3 the greatest. The black line stands for the central frequency (the real part).

It can be concluded from both the physical and mathematical points of view, that the saddle points which have small imaginary parts and also close to the carrier frequency are the ones which contribute to the electric field (Eq. (1.10)).

The simulation results obtained by the saddle point method are shown in the Fig. 4.3 at propagation distances from $60\,\mu m$ to 6 m in water and are compared with the electric field obtained from the direct integration method. The contributions of saddle points change their role as the propagation distance increases. From $60\,\mu m$ to $600\,\mu m$, the second saddle point dominates the integration. At a distance of 600 μm, the result does not match the direct integration for only a very small range of θ ($\theta > 1.36$ in Fig. 4.3 (b)) and the magnitude of the electric field is insignificant in this regime. For this condition, we can separate θ into two different regimes; for $\theta < 1.36$ we use the second saddle point while for $\theta > 1.36$ we use the third saddle point. It is more convenient to

determine the regime by setting a limit for the value of the field, because the saddle point field (Eq. (1.33)) becomes very intensive, for example, the perpendicular green lines for $\theta > 1.36$ as shown in Fig. 4.3 (b). After 600 μm, only the path integration near the third saddle point contributes to the electric field as shown in Fig 4.3 (c-f). For propagation distances greater than 6mm, the direct integration method can't provide accurate results even for the envelope. But the saddle point method still provides reasonable solutions up to a propagation distance of 6 m. And there is not much difficulty in extending the length even further.

Thus the saddle point method is more accurate than the direct integration method for a propagation distance greater than 6 mm. It is also faster computationally. The only main time consumption is solving for the saddle points. To maximize the efficiency, extra effort is required to estimate a θ window for the simulation, because for a macroscopic propagation distance, a small change of θ can lead to a great change in t for a certain z as indicated by the definition of θ.

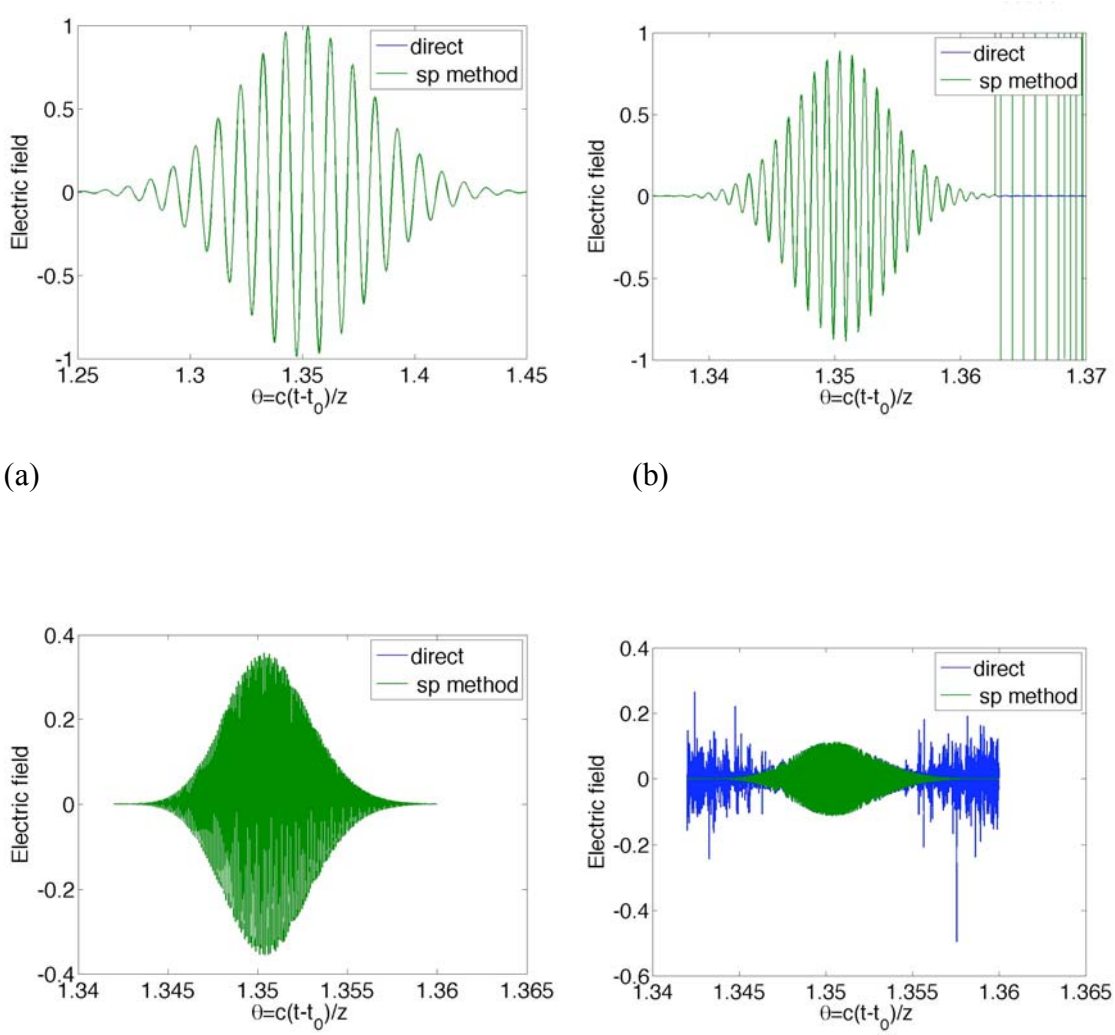

Fig. 4.3 (color online) Comparison of the results obtained by the direct integration (blue color) method and the saddle point method (green color) (direct and sp method in the legend).

(a) $z = 10^2 \lambda_c = 0.06mm$ (b) $z = 10^3 \lambda_c = 0.6mm$

(c) $z = 10^4 \lambda_c = 6mm$ (d) $z = 10^5 \lambda_c = 60mm$

(e) $z = 10^6 \lambda_c = 600mm$ (f) $z = 10^7 \lambda_c = 6000mm$

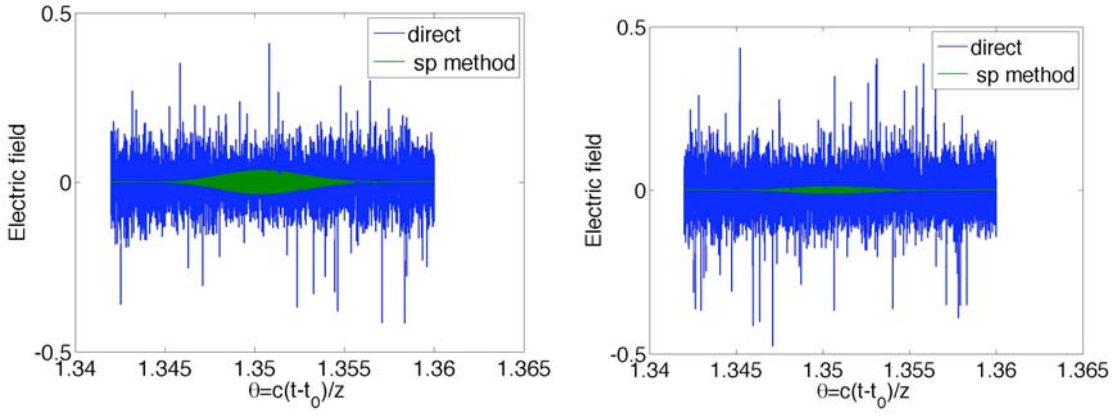

(e) (f)

Fig. 4.3 continued.

B. The GVD approximation

The convenience of the saddle point method in solving for electric fields provides a way to estimate the valid regime of the group velocity dispersion (GVD) approximation for water by comparison of pulse durations based on the GVD (or linear dispersion) approximation and the actual dispersion. For a Gaussian profile pulse, the GVD approximation leads to an analytic solution for the electric field and thus the pulse duration.

The phase delay between different spectral components determines the dispersion and thus the broadness of the pulse. Using the carrier frequency ω_c as reference, the phase can be expressed in Taylor expansion:

$$(izb_1 - it)(\omega - \omega_c) + (\frac{izb_2}{2})(\omega - \omega_c)^2 + \dots , \tag{4.7}$$

where $b_j = \left.\frac{d^j k(\omega)}{d\omega^j}\right|_{\omega=\omega_c}$, $j = 1,2,3....$ The GVD approximation keeps the expansion to second order and we define $GVD = \left.\frac{d^2 k}{d\omega^2}\right|_{\omega=\omega_c}$. Therefore the value of GVD equals b_2. By replacing the phase by the GVD approximation and using the spectrum (4.4) in Eq. (1.10), an analytic solution of the electric field is obtained:

$$E(z,t) \sim \mathrm{Re}(\exp[\frac{(t - zb_1)^2}{4(a - \frac{izb_2}{2})}]). \tag{4.8}$$

The intensity envelope is:

$$I(z,t) \sim \exp[-\frac{2a(t - zb_1)^2}{4a^2 + z^2 {b_2}^2}]. \tag{4.9}$$

Recall that $b_2 = GVD$, $a = \frac{{\tau_0}^2}{8\ln(2)}$, and pulse duration is defined as the full width at half maximum (FWHM) of the intensity, we are led to a hyperbolic relation between the pulse duration τ and the propagation distance z

$$\tau(z) = \sqrt{{\tau_0}^2 + (\frac{4\ln(2)GVD}{\tau_0})^2 z^2} \quad , \tag{4.10}$$

where $GVD = \left.\frac{d^2 k}{d\omega^2}\right|_{\omega=\omega_c}$, and GVD is the group dispersion velocity in fs^2 / mm.

For a large z, the dependence of pulse duration versus propagation distance is linear:

$$\tau(z) \approx \frac{4\ln(2)GVD}{\tau_0} z \ . \tag{4.11}$$

By applying the saddle point method for a very long propagation distance, we can calculate electric field and pulse duration. In Fig. 4.4, we compare pulse durations obtained by the GVD approximation and the saddle point method using the actual

dispersion function. The valid regime of the GVD approximation is important for the estimation of pulse duration and phase compensation by using low order dispersion. The higher order dispersion becomes significant only for long propagation distances. The simulation results show that, up to a 6 m propagation distance in water, the percentage error of the pulse durations is within 2% as shown in Fig. 4.5. Therefore, we conclude that for a medium with a flat refractive index such as water, the GVD approximation is sufficient for a propagation distance of several meters.

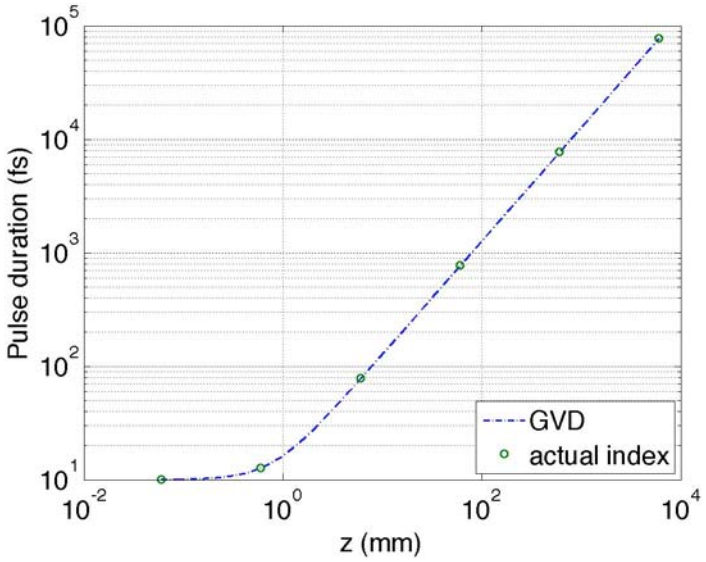

Fig. 4.4 (color online) Comparison of pulse durations obtained by the GVD approximation and the saddle point method.

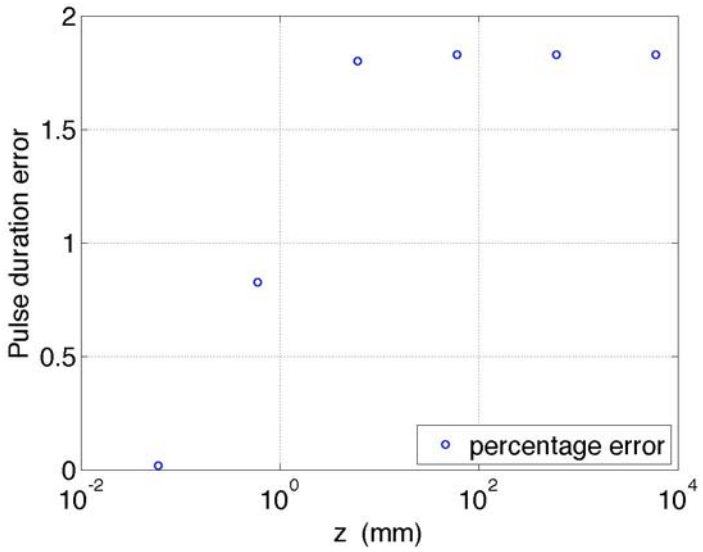

Fig. 4.5 (color online) Percentage error of pulse duration obtained by the GVD approximation method. The error is calculated with respect to pulse duration obtained by the actual dispersion function.

CHAPTER V

SUMMARY AND CONCLUSIONS

There are two categories of precursors, shown in Brillouin's book. The Sommerfeld precursor is the forerunner with high frequency components and the Brillouin precursor is the forerunner with low frequency components. Brillouin applied the saddle point method to investigate the wave front of a step-modulated signal which propagates with a velocity near the speed of light in a Lorentz medium. Oughstun 's work is more general. He applied the saddle point method to solve a Gaussian profile pulse propagating in a Lorentz medium, which leads to the so-called generalized Sommerfeld and Brillouin precursors [25]. The generalized Sommerfeld precursor in [25] propagates faster than the Brillouin precursor because the high frequency component has a greater group velocity. Therefore, the concept of precursors used by Oughstun is different from the original forerunner defined by Sommerfeld and Brillouin. The forerunners can only be observed for a pulse with a very sharp rise time, as indicated by Brillouin. The conclusion of Österberg [9] that the precursor could propagate with less than exponential attenuation is also not reasonable. Our experimental results verify that light transmission in the linear regime follows the BLB law. Theoretical study and simulation results also show that there are no conflicts between the BLB law and the existence of precursors.

Compared with the FDTD [15] method and discontinuous Galerkin method [18], for which efficient algorithms are developed only for the Debye and Lorentz dielectric medium, the saddle point method provides a fast, efficient and analytic way to solve the pulse propagation problem in a general medium. This method works well for a Lorentz

medium which has a sharp absorption line and a steep dispersion distribution and works even better for a medium such as water which has a relatively flat refractive index distribution. The accuracy is much higher than the direct integration method for a propagation distances greater than 6 mm based on the simulation of a 10 fs Gaussian profile pulse centered at 600 nm. Therefore, we conclude that the saddle point method is a very general method. By applying this method, we can compare the pulse durations given by the GVD approximation and those obtained by the actual refractive index and the error is within 2% up to a propagation distance of 6 m in water.

REFERENCES

[1] L. Brillouin, *Wave Propagation and Group Velocity* (Academic, New York, 1960).

[2] S. Chu and S. Wong, "Linear pulse propagation in an absorbing medium," Phys. Rev. Lett. **48**, 738 (1982).

[3] C. G. B. Garrett and D. E. McCumber, "Propagation of a Gaussian light pulse through an anomalous dispersion medium," Phys. Rev. A **1**, 305 (1970).

[4] M. D. Crisp, "Propagation of small-area pulses of coherent light through a resonant meium," Phys. Rev. A **1**, 1604 (1970).

[5] M. D. Crisp, "Concept of group velocity in resonant pulse propagation," Phys. Rev. A **4**, 2104 (1971).

[6] R. London, "The propagation of electromagnetic energy through an absorption dielectric," J. Phys. A **3**, 233 (1970).

[7] H. Xiao and K. E. Oughstun, "Failure of the group-velocity description for ultrawideband pulse propagation in a causally dispersive, absorptive dielectric," J. Opt. Soc. B **16**, 1773-1785 (1999).

[8] K. E. Oughstun and G. C. Sherman, *Electromagnetic Pulse Propagation in Causal Dielectric Dielectri*cs (Springer 2002).

[9] S. H. Choi and U. Österberg, "Observation of optical precursors in water," Phys. Rev. Lett. **92**, 193903 (2004).

[10] U. J. Gibson and U. Österberg, "Optical precursors and Beer's law violations: non-exponential propagation losses in water," Opt. Express. **13**, 2105-2110 (2005).

[11] A. E. Fox and U. Österberg, "Observation of non-exponential absorption of ultra-fast pulses in water," Opt. Express. **14**, 3688-3693 (2006).

[12] J. C. Li, D. R. Alexander, H. Zhang, U. Parali, D.W. Doerr, J. C. Bruce III, and H. Wang, "Propagation of ultrashort laser pulses through water, " Opt. Express **15**, 1939-1945 (2007).

[13] Y. Okawachi, A. D. Slepkov, I. H. Agha, D. F. Geraghty, and A. L. Gaeta, "Absorption of ultrashort optical pulses in water," J. Opt. Soc. Am. A **24**, 3343-3347 (2007).

[14] J. D. Jackson, *Classical Electrodynamics* (Wiley 1998).

[15] A. Taflove, and S. C. Hagness, *Computational Electrodynamics* (Artech House 2000).

[16] R. M. Joseph, S. C. Hagness and A. Taflove, "Direct time integration of Maxell's equations in linear dispersive media with absorption for scattering and propagation of femtosecond electromagnetic pulses," Opt. Lett. **16**, 18 (1991).

[17] M. Okoniewski, IEEE Microwave and Guided Wave Lett **7**, 5 (1997).

[18] J. S. Hesthaven and T. Warburton, *Nodal Discontinuous Galerkin Methods* (Springer 2008).

[19] F. Shubitidze and U. Österberg, "Phenomenological model to fit complex permittivity data of water from radio to optical frequencies," Phys. Rev .E. **75**, 0446608 (2007).

[20] E. T. Copson, *Asymptotic Expansions* (Cambridge Univ. Press 1971).

[21] L. Kou, D. Labrie, and P. Cheylek, "Refractive indices of water and ice in the 0.65-2.5 μm spectral range," Appl. Opt. **32**, 3531-3540 (1993).

[22] R. M. Pope and E. S. Fry, "Absorption spectrum (380-700 nm) of pure water. II. Integrating cavity measurements," Appl. Opt. **36**, 33, 8710-8723 (1997).

[23] L. M. Naveira, B. D. Strycker, J. Wang, G.O. Ariunbold, A.V. Sokolov, and G.W. Kattawar, "Propagation of femtosecond laser pulses through water in the linear absorption regime," Appl. Opt. **48**, 1828-1836 (2009).

[24] "Optical Glass Data Sheets," Schott, Inc., Nov. 2009, http://www.us.schott.com/advanced_optics/english/download/datasheet_all_us.pdf.

[25] K. E. Oughstun and C. M. Balictsiss, "Gaussian pulse propagation in a dispersive, absorbing dielectric," Phys. Rev. Lett. **77**, 2210-2213 (1996).

[26] X. Quan and E. S. Fry, "Empirical equation for the index of refraction of seawater," Appl. Opt. **34**, 18, 3477-3480 (1995).

[27] P. D. T. Huibers, "Models for the wavelength dependence of the index of refraction of water," Appl. Opt. **36**, 3785-3787 (1997).

VITA

Jieyu Wang was born in Jiangxi province in the middle of China. She received her Bachelor of Science degree in year 2007 from the Physics Department at The University of Science and Technology of China in Hefei, Anhui, China. She received her Master of Science degree in December 2009. Her research interests include ultrashort pulse propagation in the linear regime. Ms. Wang may be reached by email at jywangustc@tamu.edu or

Dr. George W. Kattawar

Physics Department

Texas A&M University

College Station, TX, 77843-4242.

The typist for this thesis was the author.